Deep-Sea Research Part I 124 (2017) 73–92

Contents lists available at ScienceDirect

Deep-Sea Research Part I

journal homepage: www.elsevier.com/locate/dsri

An improved near-surface velocity climatology for the global ocean from drifter observations

Lucas C. Laurindo[a,*], Arthur J. Mariano[a], Rick Lumpkin[b]

[a] Rosenstiel School of Marine & Atmospheric Science, University of Miami, 4600 Rickenbacker Causeway, Miami, FL 33149, USA
[b] NOAA/Atlantic Oceanographic and Meteorological Laboratory, 4301 Rickenbacker Causeway, Miami, FL 33149, USA

ARTICLE INFO

Keywords:
Near-surface velocity climatology
Ocean drifters
Gauss-Markov estimation
Drifter slip bias
Error analysis

ABSTRACT

This work updates the methods of Lumpkin and Johnson (2013) to obtain an improved near-surface velocity climatology for the global ocean using observations from undrogued and 15-m drogued Global Drifter Program (GDP) drifters. The proposed procedure includes the correction of the slip bias of undrogued drifters, thus recovering about half of the GDP dataset; and a new approach for decomposing Lagrangian data into mean, seasonal and eddy components, which reduces the smoothing of spatial gradients inherent in data binning methods. The sensitivity of the results to method parameters, the method performance relative to other techniques, and the associated estimation errors, are evaluated using statistics calculated for a test dataset consisting of altimeter-derived geostrophic velocities subsampled at the drifter locations, and for the full altimeter-derived geostrophic velocity fields.

It is demonstrated that (1) the correction of drifter slip bias produces statistically similar mean velocities for both drogued and undrogued drifter datasets at most latitudes and reduces differences between their variance estimates, (2) the proposed decomposition method produces pseudo-Eulerian mean fields with magnitudes and horizontal scales closer to time-averaged Eulerian observations than other methods, and (3) standard errors calculated for pseudo-Eulerian quantities underestimate the real errors by a factor of almost two. The improved decomposition method and the inclusion of undrogued drifters in the analysis allows resolving details of the time-mean circulation not well defined in the previous version of the climatology, such as the cross-stream structure of western boundary currents, recirculation cells, and zonally-elongated mid-ocean striations.

1. Introduction

A global climatology of surface ocean currents is desirable for a variety of applications. For example, the statistical moments of the ocean velocity (mean, variance, and covariances) are used in the study of linear geophysical instabilities, ocean energetics, and the turbulent transport of tracers and heat. In a Lagrangian framework, the fluctuations around the mean are used to infer eddy diffusivities and decorrelation time scales. Besides the investigation of the underlying ocean dynamics, the statistical description of the surface circulation is also relevant for ship routing, search and rescue operations, and for predicting the dispersion and transport pathways of biogeochemical tracers and of pollutants such as oil, microplastic, and floating marine debris.

The drifters of the Global Drifter Program (GDP) currently provide the most accurate set of measurements of the near-surface ocean velocities at global scales (Lumpkin and Pazos, 2007; Maximenko et al., 2013). However, observations are scattered in space and time and often autocorrelated in both dimensions, making their decomposition into mean and fluctuating components a non-trivial exercise. A common approach involves ensemble-averaging data selected within spatial bins (e.g. Niiler, 2001; Fratantoni, 2001; Jakobsen et al., 2003; Reverdin et al., 2003; Maximenko et al., 2009; Zhurbas et al., 2014), however, this method has a number of associated biases whose effects are difficult to diagnose (Mariano and Ryan, 2007). A particularly important source of uncertainty lies in the choice of bin size, whose definition involves a trade-off between the statistical reliability of the results and the resolution of the horizontal scales of the mean flow. Specifically, larger bins select more data points, which leads to a higher statistical significance of the estimates, however they smooth horizontal variations of the mean at scales smaller than the bin. Conversely, smaller bins better resolve spatial gradients, however the use of less data points increase the estimation errors. The bin size choice, therefore, influences the estimation of the mean, consequently also affecting the residuals and thus second moment statistical properties (Fratantoni, 2001; LaCasce, 2008; Koszalka and LaCasce, 2010).

* Corresponding author.
E-mail addresses: llaurindo@miami.edu (L.C. Laurindo), amariano@miami.edu (A.J. Mariano), rick.lumpkin@noaa.gov (R. Lumpkin).

http://dx.doi.org/10.1016/j.dsr.2017.04.009
Received 13 September 2016; Received in revised form 8 April 2017; Accepted 9 April 2017
Available online 13 April 2017

Furthermore, while most studies based on binning methods employed fixed-sized bins, a consequence of this practice is obtaining pseudo-Eulerian estimates whose statistical reliability vary in space. To avoid this issue, Koszalka and LaCasce (2010) proposed selecting data in clusters covering unequal areas but with a similar number of observations. Notably, the application of this technique to GDP data in the Nordic seas resolved features of the time-mean circulation with scales ≤10 km in well-sampled regions (Koszalka et al., 2011). However, the number of observations per cluster prescribed in that work results in an average selection radius of 75 km (~0.67° latitude and ~1.3–1.8° longitude, in their study area), meaning that horizontal velocity gradients at mesoscale ranges are smoothed out when considering typical ocean sampling densities.

Another source of uncertainty is due to the fact that drifters do not perfectly track the horizontal flow. Differences between the measured velocities and the actual current velocities, an effect known as slip, are caused by wind drag on the drifters surface float and wave-induced phenomena, such as Stokes drift and drifter self-propulsion by wave surfing. GDP drifters include a drogue centered at 15-meter depth that minimizes the wind and wave-induced bias, however that also introduces another component to the slip via the vertical velocity shear between the surface float and the subsurface drogue. Despite the complex nature of the processes driving the slip motion, the drogued design of GDP drifters is calibrated to yield a predominantly downwind slip of less than ~0.1% of the 10-m wind speed, for winds up to 10 m/s (Niiler et al., 1995). An assessment of the GDP dataset by Lumpkin et al. (2013) showed that more than 50% of the available data previously believed to be from drogued drifters are actually from instruments that had lost their drogues, a condition that changes the sampling level from 15-m to the surface, and renders their trajectories more sensitive to wind and wave effects, increasing the slip to about 0.7–1.6% of the 10-m wind speed (e.g. Pazan and Niiler, 2001; Poulain et al., 2009; Peng et al., 2015b).

Nearly-global maps of the mean surface ocean circulation calculated from drifter observations using bin-averaging were presented by Niiler (2001) and Maximenko et al. (2009). Considering that these fields were biased by undrogued drifter data, and seeking to reduce the smoothing effect of data binning, Lumpkin and Johnson (2013) produced a global climatology using drogued-only observations and a new binning method that simultaneously models spatial and temporal variations. However, since the exclusion of undrogued data significantly reduces the observational density in many oceanic areas, Lumpkin and Johnson (2013) selected data within relatively large bins (specifically within ellipses oriented by the variance of the binned observations, with areas equivalent to 2° radius circles) to obtain statistically significant estimates homogeneously distributed throughout the oceans. Although the use of large bins better resolves large-scale circulation patterns, it has the potential to significantly smooth coherent structures at mesoscale ranges, such as the large cross-stream velocity gradient associated with western boundary currents.

Based on these considerations, this study applies a first-order correction to the slip of undrogued drifters by referencing their velocity estimates to 15-m using a formulation proposed by Pazan and Niiler (2001), and describes a new estimation method designed to further reduce the smoothing effect of data binning, in order to generate a new comprehensive velocity climatology at 15-m depth (hereafter referred to as “near-surface”) of the global ocean. The mean fields obtained using the proposed approach recover well-known large-scale circulation features, and resolve coherent structures at mesoscale ranges whose visualization was only possible by time-averaging surface velocities indirectly inferred from satellite observations (e.g. Lagerloef et al., 1999; Maximenko et al., 2009). A thorough description of the circulation in light of the new results, including its seasonal variations and kinetic energy distribution, will be the subject of an upcoming publication. Here, focus is given to describing the proposed method and to analyzing its associated uncertainties.

This work is organized as follows. Section 2 describes the datasets, the correction of drifter slip bias, and the method proposed for the decomposition of Lagrangian data into mean, seasonal and eddy components. Section 3 presents the results of sensitivity tests to method parameters and an error analysis, describes the improvements of the new climatological fields relative to the results of Lumpkin and Johnson (2013), and briefly describes prominent new features observed in the obtained global maps. Finally, Section 4 summarizes this study and its conclusions.

2. Methods

2.1. Data description

2.1.1. Position/velocity observations from surface ocean drifters

This analysis uses position and horizontal velocity data from both undrogued and 15-m drogued drifters of the Global Drifter Program (GDP). This dataset is archived and distributed by the Atlantic Oceanographic and Meteorological Laboratory of the National Oceanic and Atmospheric Administration (AOML/NOAA, http://www.aoml.noaa.gov/phod/dac/index.php). Its generation involves the quality control of the raw drifter position fixes, and their subsequent interpolation via kriging along their trajectories to regular 6 h intervals, at which the u and v velocity components are calculated by 12 h centered differencing the kriged positions (Hansen and Poulain, 1996). The GDP dataset obtained for this study comprises more than 29 million, six hour position/velocity estimates scattered throughout the worlds ocean, from February 1979 to June 2015. About 56% of the available data points are from undrogued drifters.

Fig. 1 shows global distribution maps of the data obtained by drogued, undrogued and both types of drifters (top, middle and bottom panels, respectively), in observation days per square degree. The density of data obtained by drogued drifters is usually higher close to continental contours and to traditional deployment sites, such as the western North Atlantic, the western and eastern North Pacific, the tropical Pacific, Sea of Japan, and near the Antarctic Peninsula, while the distribution of data from undrogued instruments marks time-averaged convergence zones in the interior of the subtropical gyres, notably highlighting garbage patches in the eastern South Pacific, and within the subtropical gyres of the Atlantic ocean. These characteristics arise because (a) the probability of drogue loss increases as a function of drifter age, with about 30% (90%) of these instruments losing their drogues within the first 3 months (1.5 years) of operation (Grodsky et al., 2011); (b) a time scale of months to years is required for drifters deployed near coastal areas to travel to the interior of the gyres, meaning that instruments sampling these regions tend to be older and thus more frequently undrogued; and (c) the drifters ultimately tend to move away from time-averaged divergence areas, such as the equatorial region, and to accumulate at convergence zones, such as the interior of subtropical gyres. While Ekman convergence plays a role in this effect, Beron-Vera et al. (2016) demonstrated that the main mechanism driving the accumulation of undrogued drifters at large-scale convergence zones is the combined action of wind and currents on finite-sized floating objects.

2.1.2. Altimeter-derived geostrophic velocity fields

Altimeter-derived surface geostrophic velocity (GV) fields are produced by the *Segment Sol Multimissions d'Altimétrie, d'Orbitographie et de Localisation Précise* of the Data Unification and Altimeter Combination (SSALTO/DUACS), and were obtained from the Archiving, Validation and Interpretation of Satellite Ocean Data (AVISO, http://www.aviso.altimetry.fr/duacs/). For its generation, regularly-gridded sea-surface height (SSH) fields are initially obtained by merging data from two altimetric satellites with different sampling characteristics. One is from the TOPEX/Jason missions, with a 315 km equatorial ground track separation and a 9.9156 days global sampling

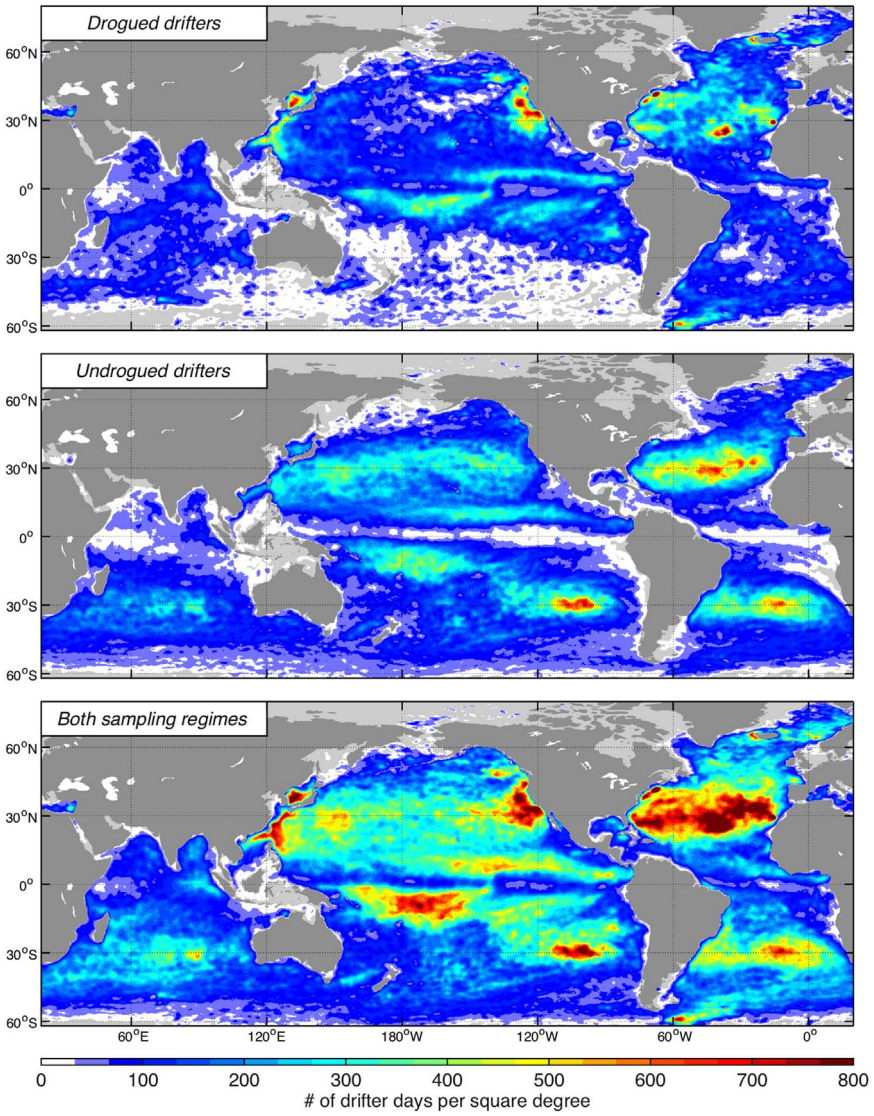

Fig. 1. Number of drifter observation days per square degree for the period between February 1979 and June 2015, considering data obtained from drogued, undrogued, and both sampling regimes (top, middle and bottom panel, respectively).

cycle, and the other is from the ERS/Envisat missions, with an 85 km equatorial ground track separation and a 35 days sampling cycle. The use of simultaneous observations from these two sampling strategies allows the generation of SSH fields with higher spatial-temporal resolution (Chelton et al., 2007), while using data from only two satellites at a time ensures a homogeneous spatial-temporal error distribution (Polito and Sato, 2015). Geostrophic velocities are then calculated at the extratropics using the geostrophic relations, and within a 5° band around the equator using a β-plane formulation of the geostrophic equations (Lagerloef et al., 1999). The time series of GV maps obtained for this study has a $0.25° \times 0.25° \times 1$ day resolution, covering the oceans between 67.5°S and 67.5°N from October 1992 until June 2015.

2.1.3. Reanalysis 10-m wind fields

10 meter height wind velocity fields are from the European Centre for Medium-Range Weather Forecasts (ECMWF, http://www.ecmwf.int) ERA-Interim reanalysis model (Dee et al., 2011). The obtained time-series of maps have a $1° \times 1°$×6 hour resolution and spans the entire temporal coverage of the GDP dataset. The use of reanalysis winds is based on the assumption that, as this class of numerical models continually assimilates real geophysical measurements to redefine their initial conditions, their results constitute the best available representation of the surface wind field in the absence of actual observations.

2.2. Correction of drifter slip bias

Due to the significant slip of undrogued drifters, previous studies recommended not using their data for calculating pseudo-Eulerian flow statistics without first correcting for slip (e.g. Grodsky et al., 2011; Lumpkin and Johnson, 2013). As shown by Fig. 1, this significantly reduces the observational density in extensive oceanic regions, particularly in the Southern Ocean, the South Pacific, and the subtropical gyres of all three major ocean basins. Methods for correcting the downwind slip of undrogued drifters are available in the literature (e.g. Pazan and Niiler, 2001; Poulain et al., 2009), whose application in the equatorial Atlantic and in the Indian Ocean reduced differences between pseudo-Eulerian statistical properties calculated using observations from each sampling regime (Perez et al., 2014; Peng et al., 2015a). Based on these considerations, this Section extends the correction of the undrogued drifter slip velocities to the global ocean, and evaluates the advantages and biases of this practice for calculating the ocean velocities' pseudo-Eulerian mean and variance.

First, the ECMWF 10-m wind fields are linearly interpolated to the

drifter locations. To account for the slip motion, a downwind velocity modeled as $\alpha \times W$ is subtracted from the drifter velocities, where W is the 10-m wind speed, and α is the fraction of W converted to the slip. For drogued instruments, $\alpha_d = 7 \times 10^{-4}$ (Niiler et al., 1995). For undrogued drifters, α_u is calculated using a formulation proposed in Pazan and Niiler (2001), given by

$$\alpha_u = \frac{<U_u> - <U_d>}{<W>} + \alpha_d, \quad (1)$$

where the subscripts d and u respectively denote drogued and undrogued drifters, U is the downwind component of the drifter velocities, and the brackets represent ensemble averages. Specifically, α_u is calculated using 6-h drogued and undrogued drifter observations selected within $4^\circ \times 4^\circ$ spatial bins centered at the grid points of a $1^\circ \times 1^\circ$ global grid. Only bins with more than 300 data points were considered, and where $<U_u> \neq <U_d>$ and $<W> \neq 0$ within 95% confidence margins, assuming for simplicity that the observations are independent. Results for α_u more than 3 standard deviations away from the mean of the results of all bins were taken as outliers, and also excluded. The latter operation was iterated 3 times to guarantee convergence of the α_u histogram distribution.

Fig. 2 shows the spatial and histogram distributions of the obtained α_u values (left and right panel, respectively). The global set of α_u retrievals have mean $\mu = 1.48 \times 10^{-2}$ and standard deviation $\sigma = 0.49 \times 10^{-2}$, where a Gaussian function fitted to the histogram (red line) indicates that this quantity can be approximately described as a normally-distributed random variable. The histogram encompasses α_u estimates of previous studies, including 0.97×10^{-2} for the Pacific and North Atlantic oceans (Pazan and Niiler, 2001), 0.66×10^{-2} in the eastern Mediterranean Sea (Poulain et al., 2009), and 1.64×10^{-2} in the equatorial Atlantic and in the Indian Ocean (Perez et al., 2014; Peng et al., 2015a). Conversely, the spatial distribution of α_u shows continuous large-scale patterns that would not be observed in the case of a purely random quantity, and that are also qualitatively different from the GDP data spatial distribution (Fig. 1). One possible explanation for the observed patterns is that they reflect the geographical distribution of drifters equipped with surface floats of different aerodynamic characteristics, that would thus react differently to direct wind forcing. However, estimates of α_u as a function of the float surface area (not shown) revealed a weak dependency between these two parameters, suggesting that the distribution in Fig. 2 reflects different geophysical conditions, and are not merely the result of random chance, heterogeneous data distribution, and/or instrument-specific properties.

It is possible that the geographical dependency of α_u seen in Fig. 2 reflects the response of the drifter velocities to a spatially-varying surface gravity wave field. This is suggested considering the fact that the correction proposed by Eq. (1) is based on how the wind affects the trajectories of drogued drifters, not accounting for the increased sensitivity of undrogued instruments to wave-induced slip motion, which preferentially aligns itself with the direction of the swell propagation rather than with the 10-m winds. Testing this hypothesis is beyond the objectives of this work, although a possible venue of investigation involves using directional wave spectra, retrieved from global ocean wave numerical models and/or from satellite-based synthetic aperture radar observations, to estimate the surface Stokes drift velocities.

The downwind slip correction applied here accounts for the spatial variations of α_u by linearly interpolating the values shown in Fig. 2 to the drifter locations. To evaluate this approach, drifter data was selected within 1° radius bins centered around the grid points of a $0.25^\circ \times 0.25^\circ$ global grid, at which the velocity's mean and variance were separately calculated for drogued and undrogued data before and after the slip correction. Fig. 3 shows the results obtained for the zonal velocity component, in terms of the longitudinal averages of the pseudo-Eulerian mean (panels a and b) and variance (c, d). Panel (e) highlights the undrogued/drogued variance ratio before and after the correction.

Fig. 3a shows that the mean velocities estimated using uncorrected data can differ by $\mathcal{O}$[0.1 m/s] due to the increased slip of undrogued drifters. This bias is visible across all latitudes, predominantly reflecting the magnitude and direction of the mean 10-m zonal winds, and is particularly intense in the Southern Ocean, where the undrogued drifter mean velocities can be a factor of two bigger than those estimated from drogued instruments. Accounting for the downwind slip virtually eliminates these differences, leading to time and zonally-averaged velocities for drogued and undrogued drifters that are statistically identical within 95% confidence margins across most latitudes (Fig. 3b).

For the variances, a visual comparison between Fig. 3c and d, and between the orange and black lines in Fig. 3e, shows that the values calculated using observations from undrogued drifters surpasses those from drogued instruments at most latitudes both before and after the slip correction, although the operation does significantly reduce their differences. In terms of global averages, the correction reduces the undrogued/drogued variance ratio from 1.88 to 1.36. Section 3.2 demonstrates that the remaining discrepancies can be largely attributed to factors unrelated to slip motion, such as the reduced sampling density of drogued drifters, methodological errors, and possible sampling biases of drogued and undrogued instruments.

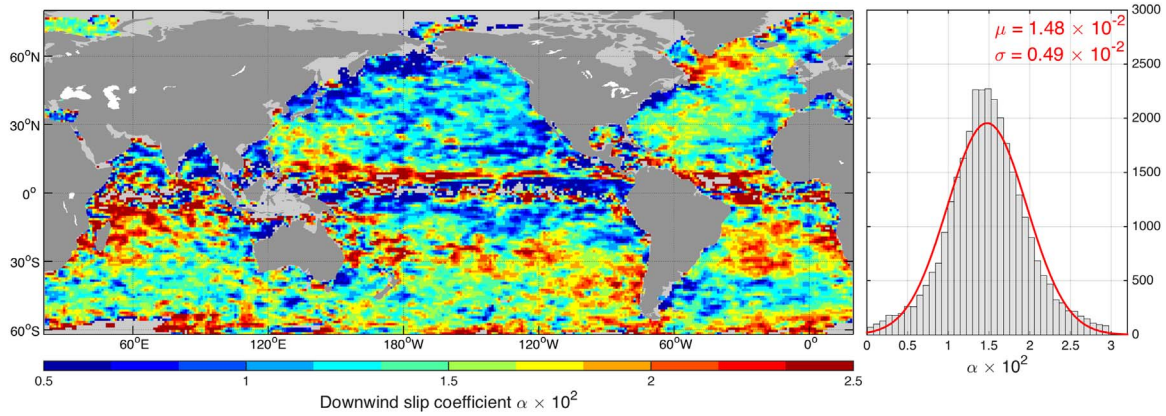

Fig. 2. Downwind slip coefficient for undrogued GDP drifters α_u calculated via Eq. (1), using velocity observations from drogued and undrogued GDP drifters and 10-m wind data from the ECMWF ERA-Interim reanalysis selected within $4^\circ \times 4^\circ$ bins, centered on the grid points of a $1^\circ \times 1^\circ$ global grid. Left: global map of the retrieved α_u values. Right: histogram of this parameter, where the red line is a Gaussian function fitted to the α_u distribution. (For interpretation of the references to color in this figure legend, the reader is referred to the web version of this article.)

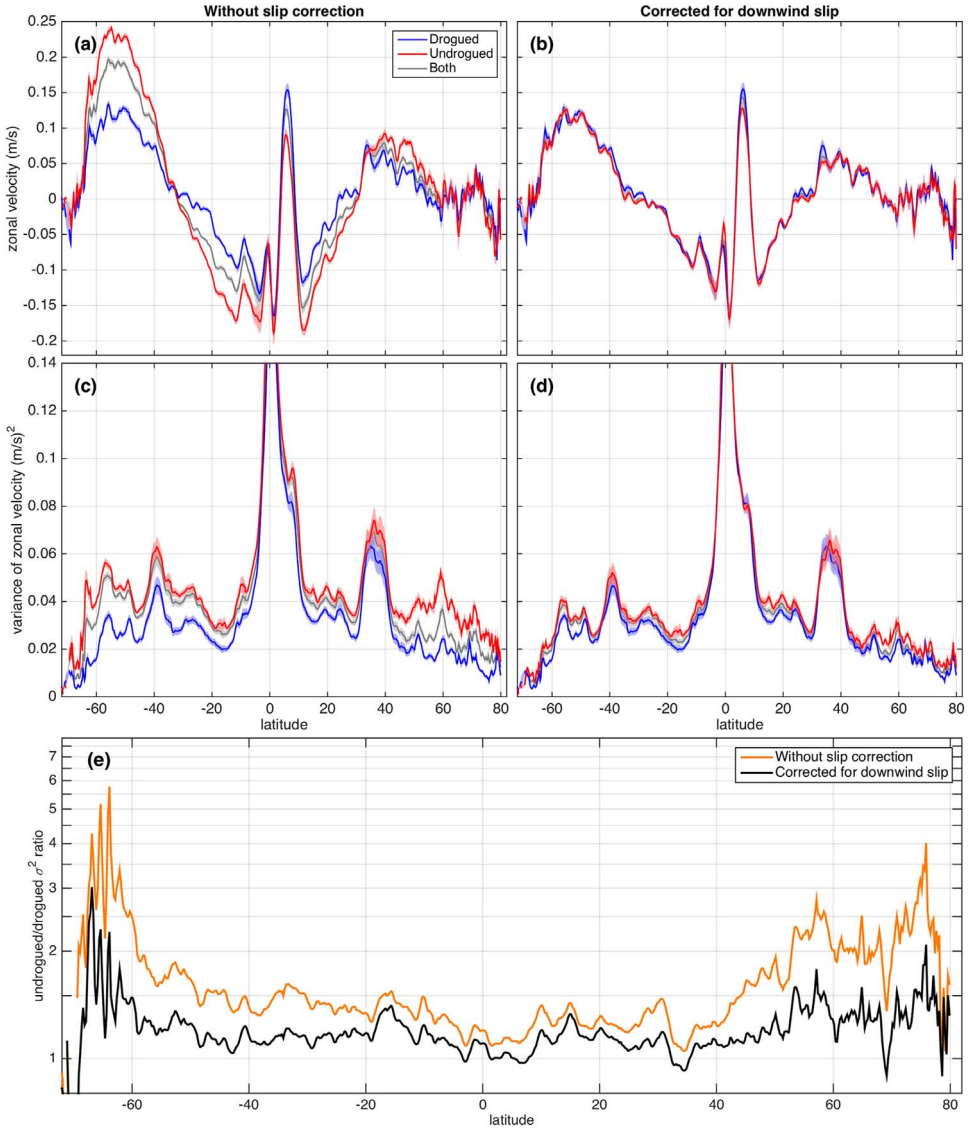

Fig. 3. Longitudinal average of the pseudo-Eulerian mean (panels a and b) and variance (c and d) for the zonal ocean velocities, estimated from drifter observations. The blue, red and gray lines are calculated using data from drogued, undrogued and both drifter types, respectively; shading around each line denotes 95% confidence intervals. The left panels (a, c) are obtained without accounting for drifter slip bias, while the right (b, d) are based on drifter velocities corrected for downwind slip, following the methods described in the text. Panel (e) shows the zonally-averaged undrogued/drogued variance ratio before and after correction (orange and black line, respectively). (For interpretation of the references to color in this figure legend, the reader is referred to the web version of this article.)

2.3. Decomposition of Lagrangian data

2.3.1. Proposed method

Following Lumpkin and Johnson (2013), the slip-corrected 6-h drifter velocities are preliminarily low-pass filtered along the trajectories using a 5th degree Butterworth filter with a cutoff period at 1.5 times the local inertial period or five days, whichever is shorter, to remove tidal and near-inertial variability, and then linearly interpolated to daily values, considering the fact that 6-h measurements are not independent within the Lagrangian integral time scale, estimated to be between 2 and 3 days. Although a 1-day resolution is still within this range, it reduces the amount of correlated data used in subsequent operations without significantly impacting the data coverage in sparsely sampled areas of the ocean.

Data subsets of the zonal and meridional drifter velocities, u and v, are then selected within circular spatial bins centered on the grid points of a $0.25° \times 0.25°$ global grid. The bins have a radius equivalent to 1° longitude, meaning that they overlap each other by 0.75° in the zonal direction and that their area decreases poleward. The use of overlapping bins on a fixed Eulerian grid and the latitudinal dependence of their area seeks to increase the spatial resolution of the pseudo-Eulerian maps, and to reflect the poleward reduction of the Rossby deformation radius (Lumpkin and Johnson, 2013).

Within each bin, u and v observations are treated as data series dependent on horizontal and temporal coordinates, $V(x, y, t)$, that can be expanded as

$$V(x, y, t) = <V> + \widehat{V}(x, y) + V^s(x, y, t) + V^e(x, y, t), \quad (2)$$

where $<V>$ is an ensemble average, $\widehat{V}(x, y)$ describes horizontal variations of the mean structure, $V^s(x, y, t)$ models seasonal variations, and $V^e(x, y, t)$ are residual (eddy) fluctuations.

To estimate $\widehat{V}$, previous studies fitted 2-D functions to the binned data (e.g. Bauer et al., 1998; Johnson, 2001; Lumpkin and Johnson, 2013; Peng et al., 2015a). Although this improves the definition of horizontal velocity gradients relative to bin-averaging (e.g. Fratantoni, 2001; Jakobsen et al., 2003; Reverdin et al., 2003; Zhurbas et al., 2014), the retrieved pseudo-Eulerian mean velocity fields are still visually smooth when compared against mean maps obtained from

true Eulerian records, such as satellite products and numerical model outputs. To further reduce the smoothing, this work uses 1-D functions to model $\hat{V}$.

The 1-D approach is based on the premise that horizontal variations of the time-mean ocean velocity field are highly anisotropic, with larger scales along the mean velocity isolines than across them (Huang et al., 2007). Given that the sharpest horizontal gradients of the general ocean circulation, those associated with western boundary currents, occur along mesoscale ranges, then the mean velocity structure within mesoscale bins can be approximately described as a function of the distance across the time-mean velocity isolines. The advantage of 1-D over 2-D functions lies in the fact that their fitting requires the determination of a smaller number of coefficients, making it less prone to estimation errors due to numerical instability, and at the same time that allowing the use of more complex functions to model mean horizontal gradients.

This work uses 1-D polynomials to retrieve $\hat{V}$, and a linear combination of harmonics to model V^s. Substituting these in Eq. (2) and assuming a data subset with N observations, $V_p(\hat{x}, t)$, $p = 1, 2, 3, \ldots, N$, a system with N linear equations can be defined as

$$V_p(\hat{x}, t) = \sum_{i=0}^{n} a_i(\hat{x})^i + \sum_{j=1}^{m}\left[b_j \sin\left(\frac{\theta t}{j}\right) + c_j \cos\left(\frac{\theta t}{j}\right)\right] + V_p^e(\hat{x}, t). \tag{3}$$

The first term on the right-hand side is the nth degree polynomial function used to describe spatial gradients, with a_i, $i = 0, 1, 2, \ldots, n$, as coefficients, where $\hat{x}$ denotes the coordinate system for the 1-D fitting. The $\hat{x}$ axis is expressed as the distance in km to the data centroid (i.e. the average position of all data points) normalized by the standard deviation of all distances, and is found separately for u and v by rotating the binned observations' coordinates in angle increments of 4° about the data centroid. At each angle, the 1-D polynomial is least-squares fitted to the data sorted along the rotated x-axis and a fitting error is calculated, with the axis $\hat{x}$ being defined at the angle with the smallest error. This procedure is illustrated in Fig. 4, using v measurements selected within a 0.5° radius bin in the Florida Current. The transition from panel (a) to (b) shows that the variance relative to the fitted function (red line) is minimized when the rotated x-axis aligns with the axis of the current. The second term in the right-hand side of Eq. (3) is the harmonical expansion used to model seasonal fluctuations, where m is the number of harmonics; t is the temporal coordinate, in years; θ is the frequency of the annual cycle; and b_j and c_j, $j = 1, 2, 3, \ldots, m$, are the coefficients of the sine and cosine components of each harmonic.

For the generation of the global climatology presented in this work, the parameters n and m are set to 4 and 2, respectively, resulting in nine coefficients to be estimated in Eq. (3).

The system defined by Eq. (3) can be written in matrix form as $V = Az + V^e$, where A is a $N \times 9$ matrix containing the polynomial and periodic functions; z is a column vector holding their 9 unknown coefficients; and V^e is a column vector with N elements containing the fitting error, which is a sum of eddy velocities, observational errors, and model errors from assuming (3). Following Lumpkin (2003) and Lumpkin and Johnson (2013), a best-fit solution for z is obtained via Gauss-Markov estimation (GME) (Wunsch, 1996), an inverse curve fitting method that accounts for the fact that Lagrangian observations are correlated within the Lagrangian integral time scale, and therefore do not correspond to independent realizations of the velocity field. The variance-covariance matrix of the eddy residuals is defined prior to the fitting operation (a priori) by assuming an idealized autocovariance function, which corrects the number of degrees of freedom for the fitting and thus reduces biases caused by the use of non-independent data points (Lumpkin, 2003). The GME solution for z is

$$z = R_z A^{\mathrm{T}}(AR_zA^{\mathrm{T}} + R_n)^{-1}V, \tag{4}$$

where R_z and R_n are respectively variance-covariance matrices for the system's coefficients and eddy fluctuations, both defined a priori; and the superscript "T" denotes transposed matrices. R_z is an 9×9 matrix, whose diagonal terms are assumed to be equal to the squared difference between the maximum and minimum binned velocity values (i.e. the square of the data range), while off-diagonal terms are set to zero. R_n has $N \times N$ dimensions, and is built using the following autocovariance function,

$$R_n = \sigma_V^2 \cos\left(\frac{\pi t}{2T_d}\right) \exp\left[-\left(\frac{\pi t}{2\sqrt{2T_d}}\right)\right], \tag{5}$$

where $\sigma_V{}^2$ is the data variance, and T_d is a decorrelation time scale, set to 6.33 days, corresponding to a Lagrangian integral time scale of 3 days (Lumpkin, 2003; Lumpkin and Johnson, 2013). Furthermore, off-diagonal values of R_n are multiplied by 0.9, under the assumption that 10% of the eddy variance is due to white noise and thus uncorrelated from one observation to the next. Finally, it is assumed that observations of different drifters are always independent, meaning that the autocorrelated structure is only calculated along individual trajectories. Once the mean structure and the seasonal fluctuations are estimated, they are subtracted from the binned velocity observations to obtain the

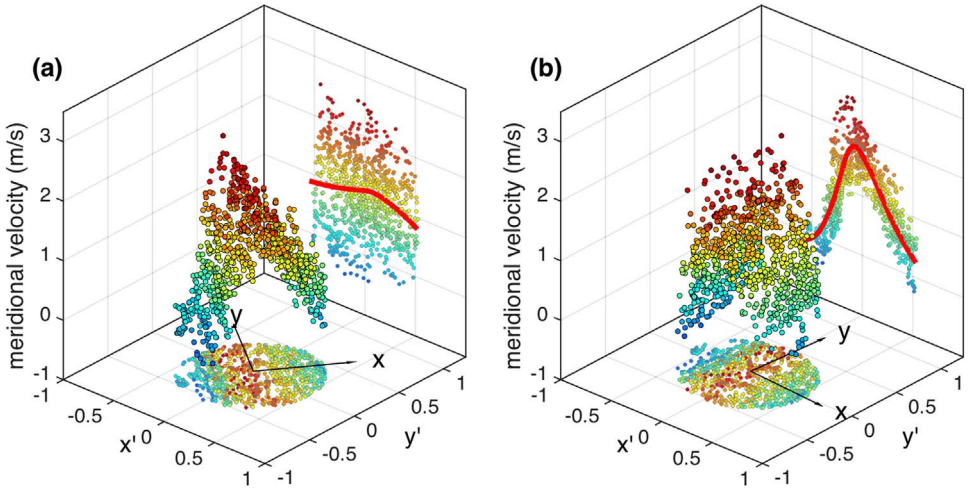

Fig. 4. Schematic representation of the 1-D curve fitting to drifter velocity data organized along the rotated x-axis. The dots are meridional velocity measurements selected within 0.5° of the coordinates 28°N, 79.75°W, region dominated by the northward flow of the Florida Current. The arrows labeled x, y show the orientation of the original Cartesian coordinate system, while x', y' are the rotated axes. In both diagrams, data is projected to the plane (x', v), along which the 1-D function is fitted (red lines). The transition from panel (a) to (b) shows that the data variance relative to the fitted function is minimized when x' is aligned with the current's mean velocity structure. (For interpretation of the references to color in this figure legend, the reader is referred to the web version of this article.)

eddy residuals V^e.

Spurious pseudo-Eulerian estimates can arise due to low observational densities. Assuming a 3-day Lagrangian integral time scale, a minimum of 60 drifter observation days (10 degrees of freedom) is required to estimate the 9 coefficients of Eq. (3). To minimize sampling-related errors, the coefficients of the periodic functions b_j and c_j are not estimated in bins with 40–90 data points, and no calculations are made in bins with less than 40 data points. However, even if such requirements are met, the fitting can be numerically unstable and produce spurious results. Thus, solutions for z are considered valid if their absolute values are smaller than the data's velocity range, and if more than 70% of the eddy residuals lies within two standard deviations of the data's ensemble mean. Failing these criteria, the fitting operation is tentatively redone using progressively smaller polynomial degrees, to a minimum of one (where only the ensemble mean $<V>$ is calculated). If valid estimates are still not obtained, the grid point is assigned a no data flag.

For mapping purposes, the best-fit coefficients of the spatial and seasonal functions are evaluated at the center of each bin, i.e., at the grid points of the $0.25° \times 0.25°$ grid. However, due to heterogeneous data distribution and the use of overlapping bins, the bin center can lay outside of the region covered by the selected data. With that in mind, an elliptical area is defined for each bin, with major and minor axes respectively equal to twice the length of the first and second eigenvalues of the data (x,y) coordinates, and rotated by the declination angle of the first eigenvalue. If the bin center lies outside this ellipse, the grid point is also assigned a no data flag.

Finally, to assess the statistical reliability of the modeled velocities, an *a posteriori* error variance-covariance matrix P_z is obtained by

$$P_z = R_z - R_z A^{\mathrm{T}} (A R_z A^{\mathrm{T}} + R_n)^{-1} A R_z, \tag{6}$$

where P_z is a 9×9 matrix, and the square root of its diagonal terms are the standard errors of the best-fit coefficients a_i, b_j and c_j. It is noted that off-diagonal (covariance) terms in P_z are different from zero, meaning that the coefficients have correlated errors. P_z can be used to obtain a variance-covariance error matrix P_n for the modeled velocities via error propagation

$$P_n = A P_z A^{\mathrm{T}}. \tag{7}$$

Here, P_n is $N \times N$, and the square root of its diagonal terms correspond to standard errors (ϵ_{SE}) for the velocity estimates. In this study, the ϵ_{SE} of the mean and seasonal velocity estimates are analyzed separately. Specifically, errors for the mean are evaluated at the bin center, coinciding with the mapped mean velocities, using only variance-covariance terms in P_z associated with the polynomial coefficients in Eq. (3), while errors for the seasonal fluctuations are evaluated at the spatial-temporal positions of the binned observations using the remaining variance-covariance terms in P_z, associated with the coefficients of the periodic functions in (3), and cross-terms between coefficients of polynomial and periodic functions.

2.3.2. Decomposition evaluation

To evaluate the performance of the decomposition method described in Section 2.3.1, altimeter-derived geostrophic velocities (GV) from AVISO are linearly interpolated to the GDP drifter locations. The proposed approach assumes that the statistical properties of the AVISO GV fields are perfect Eulerian references for estimating the errors of pseudo-Eulerian quantities calculated from the Lagrangian GV dataset.

This analysis is motivated by the fact that the decomposition method requires choices for the bin size/mapping resolution, and for the curve fitting parameters n, m, and T_d, whose definition affects the results. Furthermore, previous studies employed different decomposition methods and a wide range of bin sizes and grid resolutions, also using different Lagrangian datasets and/or data processing steps, implying that an objective comparison between methods should use the same Lagrangian dataset and averaging resolution. Finally, standard errors (ϵ_{SE}) obtained from Eq. (7) are scaled as $(\sigma^2/N)^{1/2}$, where σ^2 is the data variance and N is the number of independent samples. This means that ϵ_{SE} estimates ignore errors introduced by, for example, the spatial smoothing effect of data binning, and to possible inadequacies of physical model proposed by Eqs. (3) and (5), and therefore can differ from the actual estimation errors.

It is noted that the pseudo-Eulerian statistical properties of the Lagrangian GV data differ from those of actual drifter observations, due to the following: (1) the GV estimates are subject to uncertainties of the geoid and the global tidal models used to reference the altimetric SSH measurements, which respectively introduce errors in the velocities' magnitude and direction, and reduce the accuracy of the estimates in regions shallower than 1000 m, due to regional tidal effects forced by the local bathymetry and continental contours; (2) ageostrophic flows are absent, and the geostrophic approximation may not properly describe the circulation within coherent mesoscale eddies, which an increasing body of literature suggests to be predominantly in cyclogeostrophic balance (e.g. Castelão and Johns, 2011; Maximenko et al., 2013); and (3) the relatively large correlation length scales (ℓ[10^2 km]) assumed for the generation of regularly-gridded SSH fields implies that variability at smaller scales are underestimated (e.g. Ducet et al., 2000; Poje et al., 2014). Despite these limitations, the altimeter-derived geostrophic velocities have variance levels comparable to those estimated from in situ data (Ducet and Le Traon, 2001), implying that statistical quantities calculated from the Lagrangian GV dataset and from actual drifter velocity measurements should have similar variability.

Specifically, the Eulerian time-series of the u and v components of the AVISO geostrophic velocities at each grid point, $V(t)$, are decomposed as

$$V(t) = \overline{V} + V^s(t) + V^e(t), \tag{8}$$

where $\overline{V}$ is the long-term mean; V^s are seasonal fluctuations, estimated by least-squares fitting $m=5$ harmonics to the residuals about the mean; and V^e are eddy residuals. Variance estimates of V^s and V^e, respectively ${\sigma_s}^2$ and ${\sigma_e}^2$, are computed conventionally.

Errors (ϵ) of pseudo-Eulerian estimates of $\overline{V}$, V^s, ${\sigma_s}^2$, and ${\sigma_e}^2$, are obtained by subtracting the correspondent Eulerian values at each grid point. For simplicity, the ϵ of the u and v components are analyzed in terms of its magnitude, $\epsilon_A = \sqrt{\epsilon_u^2 + \epsilon_v^2}$, hereafter referred to as absolute errors. Due to the time dependence of V^s, its ϵ_A at each grid point is defined as the root mean square (RMS) magnitude of the errors of the seasonal velocities estimated for the binned drifter observations. Standard errors are processed similarly, to allow the comparison between ϵ_A and ϵ_{SE}.

To investigate the factors governing the horizontal distribution of ϵ_A and ϵ_{SE}, the u and v components of the reference Eulerian parameters are first used to calculate the magnitude of the mean velocity ($\overline{S} = \sqrt{\overline{u}^2 + \overline{v}^2}$, hereafter referred to as mean speed), and the kinetic energy of seasonal and eddy fluctuations (SKE and EKE, defined as the average of the respective zonal and meridional variance estimates). The retrieved ϵ_A and ϵ_{SE} are then subsampled within intervals (i.e. classes) of the correspondent Eulerian $\overline{S}$, SKE, and EKE, and simultaneously subsampled within intervals of the square roots of EKE and N. The error estimates obtained within each class are used to calculate RMS values (ϵ_A^{RMS} and ϵ_{SE}^{RMS}), allowing analyzing their variation as a function of the considered parameters.

The choices for the adjustable parameters of the proposed decomposition method were defined based on the results of this analysis, which are presented and discussed in Section 3.1. Section 3.1.1 evaluates the amount of detail recovered by pseudo-Eulerian mean velocity magnitude maps at different resolutions, while Section 3.1.2 analyze the sensitivity of the results to the fitting parameters. Section 3.1.3 shows the impact of the choice of bin size on pseudo-Eulerian

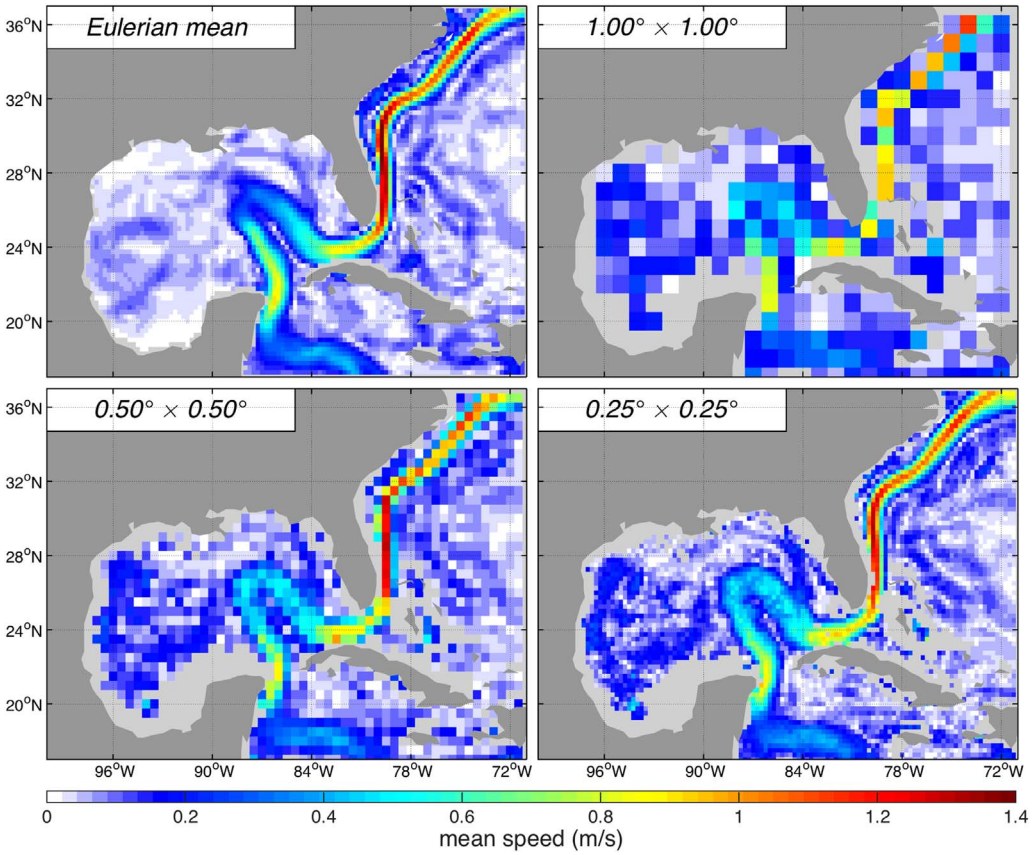

Fig. 5. Long-term average of the AVISO geostrophic speed for the Gulf of Mexico and Florida Current. The reference Eulerian field is illustrated alongside pseudo-Eulerian estimates, mapped to 1.00°×1.00°, 0.50°×0.50°, and 0.25°×0.25° grids via the 1-D GME method.

estimates, and compares the performance of the proposed decomposition method with that of other techniques. Finally, Section 3.1.4 assess the spatial distribution of errors, and compares the retrieved ϵ_A with ϵ_{SE} estimates.

3. Results and discussion

3.1. Decomposition evaluation

3.1.1. Spatial resolution of pseudo-Eulerian fields

This work maps pseudo-Eulerian estimates to a 0.25°×0.25° global grid. This resolution is adopted because it (a) corresponds to a lower bound limit required to resolve mesoscale features, and (b) coincides with the AVISO GV's native grid, allowing a comparison between pseudo-Eulerian and Eulerian statistics. However, an important question is whether the proposed decomposition method can recover horizontal velocity gradients at the scales implied by this grid. To evaluate the amount of detail recovered by pseudo-Eulerian estimates subsampled at different resolutions, Fig. 5 shows the Eulerian time-mean geostrophic speed for the Gulf of Mexico and Florida Current, alongside pseudo-Eulerian estimates obtained using data selected within 1° radius bins, and then mapped to 1°×1°, 0.5°×0.5° and 0.25°×0.25° grids.

Prominent features shown by the Eulerian field in Fig. 5 includes the Loop and Florida Currents, with mean speeds of $\mathcal{O}$[0.1–1 m/s], and smaller-scale coherent flows with $\mathcal{O}$[0.1 m/s] speeds, such as the Antilles Current and recirculation cells on the eastern flanks of the Florida and Antilles Currents. The 1°×1° field only resolves large-scale features, such as the along-stream structure of Loop and Florida Currents. At 0.5°×0.5°, the major currents are better defined and $\mathcal{O}$[0.1 m/s] features can be discerned, however the resolution is still insufficient to resolve their cross-stream velocity profiles. Further refining to 0.25°×0.25° results in circulation patterns with horizontal scales and speed magnitudes visually compatible with the reference Eulerian field, supporting the mapping resolution adopted in this work. Independent of the resolution, notable discrepancies relative to the Eulerian field are observed in the western portion of the Gulf of Mexico. Such features are attributed to low data densities (<100 data points), resulting in sparse realizations of the energetic eddy field.

3.1.2. Sensitivity to fitting parameters

The proposed decomposition technique requires a priori specifications for the parameters n and m in Eq. (3), respectively the polynomial degree and number of seasonal harmonics, and of the decorrelation time scale T_d in Eq. (5). The choice for n affects the overall adjustment of the fitted curve to the data. A low n distorts spatial features and/or underestimate their magnitudes, also reducing the sensitivity of the procedure illustrated in Fig. 4 to obtain an angle aligning with the large-scale structure of the data. Conversely, a high n may result in overfitting (i.e. the interpretation of eddy fluctuations as spatial structure), and increases the chance of estimation errors due to numerical instability.

For a quantitative evaluation, the left panel of Fig. 6 shows the ϵ_A^{RMS} of the pseudo-Eulerian mean geostrophic speed calculated as a function of the reference Eulerian values, for $n=2$, 3, 4 and 5 (red, green, black and blue lines, respectively). The shading around each line are 95% confidence margins, and the thin dashed line marks the 1:1 signal-to-noise ratio limit. The ϵ_A^{RMS} of all estimates are statistically similar for reference velocity magnitudes between 0 and 0.9 m/s, gradually rising from ~0.02 to 0.09 m/s within this interval. Above 0.9 m/s, the errors for $n=2$ ($n=3$) increase faster than for higher n, reaching ~0.32 (0.27) m/s at Eulerian speeds of 1.4 m/s. Using 4th and 5th degree polynomials, both show similar errors for speeds up to 1.2 m/s, where it reaches values of ~0.1 m/s. Past this limit, the ϵ_A^{RMS} for $n=4$ ($n=5$)

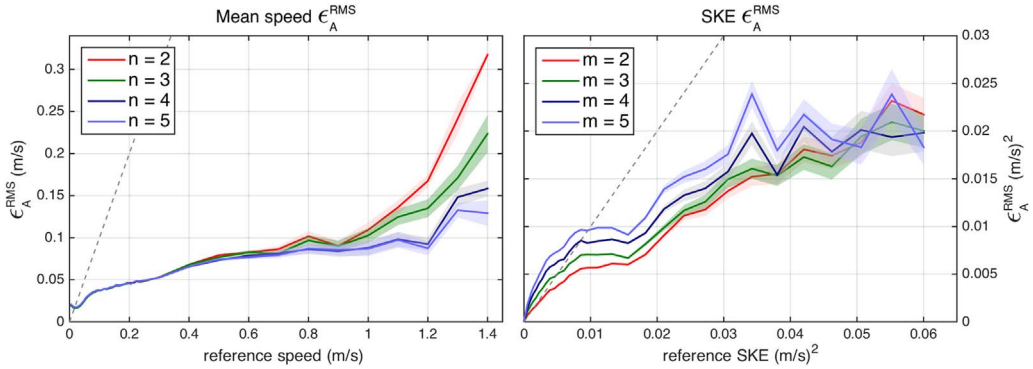

Fig. 6. Absolute errors of the pseudo-Eulerian mean geostrophic speed (left), and of the pseudo-Eulerian kinetic energy of the seasonal fluctuations (SKE) (right), calculated as a function of the correspondent Eulerian values (ϵ_A^{RMS}). n and m denotes the polynomial degree and the number of harmonics used in the model proposed in Eq. (3), while the red, green, black and blue curves correspond to values of 2, 3, 4 and 5 of each parameter. The shading around each line are 95% confidence margins, and the thin dashed line marks the 1:1 signal-to-noise ratio limit. (For interpretation of the references to color in this figure legend, the reader is referred to the web version of this article.)

further increases to 0.16 (0.13) m/s at reference speeds of 1.4 m/s. Despite the better performance of $n=5$ at higher velocities, the larger number of coefficients make the estimates more prone to stability errors and requires more data. To balance the definition of velocity gradients with the stability of the fitting operation, the climatological fields presented in this work were obtained using $n=4$.

Regarding the number of seasonal harmonics, many drifter-based studies used $m=2$, therefore resolving only annual and semiannual periods (e.g. Richardson and Walsh, 1986; Lumpkin, 2003; Lumpkin and Johnson, 2013; Peng et al., 2015b). Including more harmonics can improve the definition of the seasonal cycle, but also increases the chance of errors due to overfitting or numerical instability. To verify the sensitivity of the seasonal estimates to the choice of m, the right panel in Fig. 6 shows the ϵ_A^{RMS} of SKE calculated as a function of the correspondent Eulerian values, where the red, green, black and blue lines respectively refers to $m=2$, 3, 4 and 5. The errors calculated using $m=2$ increase from $<1\times10^{-3}$ to $\sim1.5\times10^{-2}$ m^2/s^2 for reference variances between 0 and 3.5×10^{-2} m^2/s^2. Within this range, adding one harmonic progressively increases the errors by $\sim1\times10^{-3}$ m^2/s^2 due to overfitting. For Eulerian SKE values above 3.5×10^{-2} m^2/s^2, the ϵ_A^{RMS} estimates obtained for all tested m lies within each other's error margins, varying between 1.5 and 2.5×10^{-2} m^2/s^2. Based on these results, $m=2$ is considered the optimum choice for the decomposition.

Finally, T_d is the time scale used to define independent data points in the GME method. Here, values from 0 to 20.33 days were tested. Statistically significant changes on the pseudo-Eulerian results to different T_d are not obvious in ϵ_A^{RMS} estimates as the presented in Fig. 6. However, a visual inspection of the mean speed maps show that, for $T_d\geq6.33$ days, the mean speed of features such as the Loop Current, recirculation cells, branches of the Antarctic Circumpolar Current, and the eastward extensions of the Kuroshio and Gulf Stream Currents, increase by $\mathcal{O}$[0.1 m/s] relative to results obtained for $T_d=0$. The lower speeds in $T_d=0$ are caused by a sampling bias towards smaller speeds intrinsic in data binning, arising from the fact that slower drifters tend to spend more time within a limited area than faster ones (Lumpkin, 2003; Mariano and Ryan, 2007). By defining observations as independent if they are more than 6 days apart, the relative weight of correlated low speed measurements is reduced in the curve fitting, giving higher mean speed estimates for the mentioned features (Lumpkin, 2003).

However, using $T_d>0$ also increases the chance of errors due to numerical instability. This is attributed to the fact that (a) larger T_d's reduces the number of degrees of freedom; and (b) by assuming an autocorrelated structure in time, the relative weight of the observations also change in space, which can cause estimation errors if the distribution of independent data points is asymmetric along the spatial domain. Specifically assuming $T_d=10.33$ days (as in Lumpkin and Johnson (2013)) and using the Lagrangian GV dataset, these effects caused the exclusion of estimates in $\sim$1800 grid points ($\sim$0.3% of the total), increased tenfold when using actual drifter observations due to their larger variances. To minimize such errors, a lower-bound value of $T_d=6.33$ days is adopted.

3.1.3. Sensitivity to bin size and comparison with other techniques

This section analyzes the sensitivity of pseudo-Eulerian estimates to the choice of bin size. Furthermore, since the proposed decomposition method is designed to reduce the smoothing effect of binning, its performance is compared against that of other methods, including (a) bin-averaging (e.g. Fratantoni, 2001; Jakobsen et al., 2003; Reverdin et al., 2003; Zhurbas et al., 2014); (b) 2-D polynomial fitting via GME (Lumpkin and Johnson, 2013; Lumpkin and Flament, 2013; Peng et al., 2015a); (c) least-squares smoothing 2-D cubic splines (LSS) (Bauer et al., 1998; Falco and Zambianchi, 2011); and (d) a 1-D version of the LSS spline fitting.

Following Lumpkin and Johnson (2013), a 2nd degree polynomial is used in the 2-D GME. In a brief description of the LSS method, this technique requires a priori assumptions of the smoothness level of the fitted curve, which allows more stable estimates than the traditional least-squares fit (Inoue, 1986). The LSS uses cubic splines, which are functions constituted by a set of piece-wise cubic polynomials with continuous first and second derivatives at their connection points, known as knots. The LSS fitting parameters include the number of equispaced spline knots (k), and the spline roughness and tension (ρ and τ, respectively). These were defined via sensitivity tests, resulting in ρ, $\tau=1$ for both 1-D and 2-D versions, and $k=3$ ($k=2$) for 1-D (2-D).

Fig. 7 shows pseudo-Eulerian mean geostrophic speed maps for the Loop and Florida Currents. The left, middle and right panels are calculated using circular bins with radius equivalent to 0.5°, 1° and 1.5° degrees longitude, respectively. From top to bottom, results are respectively obtained via bin-averaging, 1-D and 2-D GME polynomial fitting, and 1-D and 2-D LSS spline fitting. This region was chosen to illustrate characteristics observed in the global fields because it simultaneously includes an intense western boundary current, recirculation cells, and coherent circulation structures in the basin interior, features whose cross-stream velocity gradients are frequently smoothed in pseudo-Eulerian estimates.

The bin-averaged fields in Fig. 7 demonstrate the smoothing of spatial gradients due to the use of progressively larger bin areas. Particularly for 0.5° radius bins, the Loop and Florida Currents have cross-stream scales visually compatible with the Eulerian mean field (Fig. 5), and maximum core speeds of $\sim$1 m/s, about 0.4 m/s smaller than the Eulerian values. The Antilles Current and recirculation cells can also be observed, with mean speeds of $\mathcal{O}$[0.1 m/s]. Increasing the bin size to 1° broadens the cross-stream structure of all currents and attenuates their speeds by a factor of 2. Using 1.5° radius bins, only the largest scales of the circulation are resolved, where features such as the

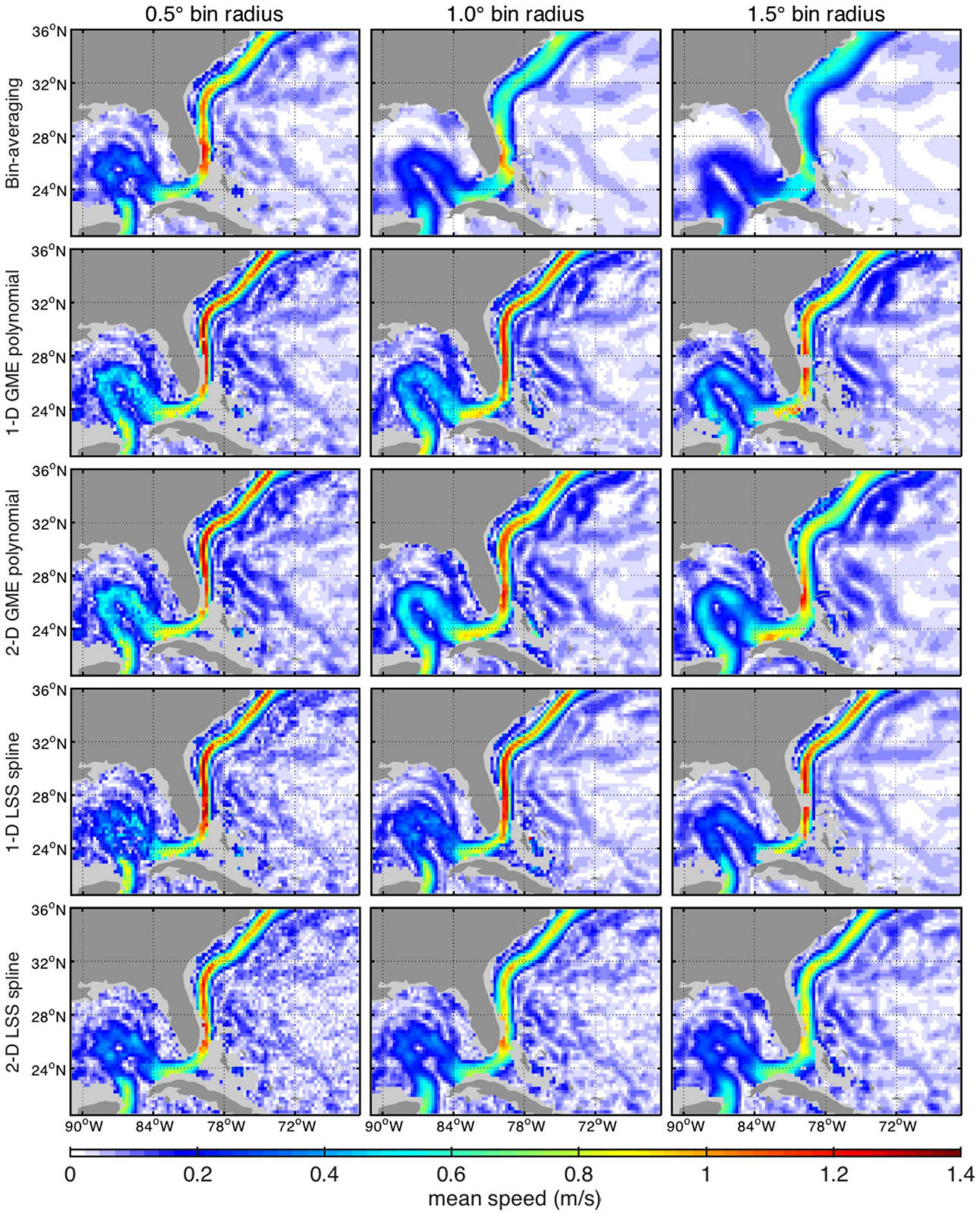

Fig. 7. Pseudo-Eulerian mean geostrophic speed estimates for the Loop and Florida Currents, obtained from data selected within circular bins with radii equivalent to 0.5° (left column), 1° (middle) and 1.5° (right) degrees longitude. From top to bottom, the mean fields were respectively calculated via bin-averaging (e.g. Fratantoni, 2001), 1-D and 2-D polynomial fitting via Gauss-Markov estimation (GME) (e.g. Lumpkin and Johnson, 2013), and 1-D and 2-D least-squares smooth spline fitting (LSS) (e.g. Bauer et al., 1998).

Antilles Current, recirculation cells, and the cross-stream structure of the Loop and Florida Currents, are either absent or significantly smoothed. Contrasting with the bin-averaged maps, the fields calculated using curve fitting methods all show circulation patterns with spatial scales and speed magnitudes visually closer to the Eulerian field.

Comparing maps in Fig. 7 calculated using 1-D and 2-D curve fitting methods, both produces visually similar results for 0.5° radius bins. However, increasing the bin radius to 1° (1.5°), the Florida Current

velocities are more strongly attenuated in the 2-D version, being specifically ~0.4 (0.5) m/s smaller in the LSS, and ~0.1 (0.2) m/s in the GME. Conversely, the fields calculated using 1-D functions have gaps (blank grid points) not observed in their 2-D correspondents, that are particularly evident in the maps obtained using 1.5° radius bins at the Florida Straits and between the Florida peninsula and the Bahamas. As described in Section 2.3.1, grid points in the proposed 1-D approach are left blank when the bin center is outside the data coverage, criteria that was not adopted when using 2-D functions.

As for differences between maps obtained via GME and LSS in Fig. 7, the GME fields show mean Loop Current speeds closer to the Eulerian values for all tested bin radii. Specifically, the reference Eulerian map in Fig. 5 show speeds between 0.4 and 0.6 m/s for the Loop Current, in contrast with the 0.2–0.4 m/s range obtained via LSS, which is similar to the observed in the bin-averaged maps. The GME method also produces larger speeds for the Antilles Current and recirculation cells, surpassing the correspondent LSS values by ~0.05 m/s. As described in Section 3.1.2, data binning preferentially samples slower drifters, introducing the observed low speed bias in the bin-averaged and LSS results (Lumpkin, 2003). The GME method reduces this effect because it redistributes degrees of freedom based on a prescribed decorrelation time scale, which reduces the relative weight of autocorrelated low-speed measurements. However, improvement is not observed in the Florida Current, where the 1-D LSS actually produces higher speeds than 1-D GME (~0.1 m/s difference, using 1.5° radius bins). This is attributed to the use of more complex functions in LSS (3-knot cubic splines), which allow a better description of the intense Florida current's cross-stream gradients than the 4th degree polynomials used in the 1-D GME.

For a quantitative analysis, Fig. 8 shows the ϵ_A^{RMS} of the global pseudo-Eulerian estimates of the mean geostrophic speed (left panels, a, c and e), and EKE (right, b, d and f), calculated as a function of the Eulerian mean speed for both parameters. The dependency of their absolute errors to the mean Eulerian speed is assumed because, as data binning attenuates horizontal velocity gradients, undiagnosed spatial structure would be interpreted as eddy fluctuations, thus introducing errors in the pseudo-Eulerian variances.

Considering first the results of bin-averaging, panel (a) of Fig. 8 shows that, using 0.5° radius bins, the ϵ_A^{RMS} of mean speed estimates of all tested decomposition methods increase from 0.02 to 0.07 m/s for Eulerian speeds between 0 and 0.7 m/s. Past this limit, the errors of the bin-averaged estimates increase faster than that of other methods, reaching 0.36 m/s at Eulerian speeds of 1.4 m/s. The ϵ_A^{RMS} values of the correspondent EKE estimates (b) increase approximately linearly as a function of the Eulerian values, varying from 0.002 to 0.04 m^2/s^2, becoming notably larger than the errors of other methods past 1.2 m/s. Panels (c) to (f) show that the errors of bin-averaged estimates of both quantities increases significantly at larger bin sizes. Particularly for 1° (1.5°) radius bins, the ϵ_A^{RMS} of mean speed estimates (c, e) exceeds that of other methods at Eulerian speeds of >0.4 (0.2) m/s, reaching maximum values of 0.77 (1.00) m/s. The larger errors in the mean are reflected in the correspondent EKE estimates (d, f), reaching maximum values of 0.11 (0.13) m^2/s^2 at Eulerian speeds of 1.4 m/s.

Although less pronounced, an increase of ϵ_A^{RMS} for larger bin sizes is also observed in results of curve fitting methods, particularly for the 2-D approach. Analyzing results from the 1-D and 2-D LSS, panels (a), (c), and (e) of in Fig. 8 shows that estimates obtained by the 2-D version have consistently larger errors than 1-D for Eulerian speeds >0.6 m/s, for all bin radii. Specifically, mean speed obtained by the 2-D LSS show ϵ_A^{RMS} values of 0.26, 0.47 and 0.52 m/s (respectively for 0.5°, 1° and 1.5° radius bins) at Eulerian speed of 1.4 m/s, against 0.07, 0.10 and 0.13 m/s for the 1-D LSS. Panel (b) shows that the EKE errors for 1-D and 2-D LSS are statistically similar to each other for 0.5° radius bins, increasing from 0.002 to 0.035 m^2/s^2 for up to 1.2 m/s reference speeds, and decreasing to 0.002 m^2/s^2 at 1.4 m/s. For 1° (1.5°) radius bins (d, f), the ϵ_A^{RMS} of EKE estimates of both 1-D and 2-D versions are similar along most of the Eulerian speed range, reaching maximum values of ~0.04 m^2/s^2 within the 0.8–1.2 m/s range. For reference speeds above

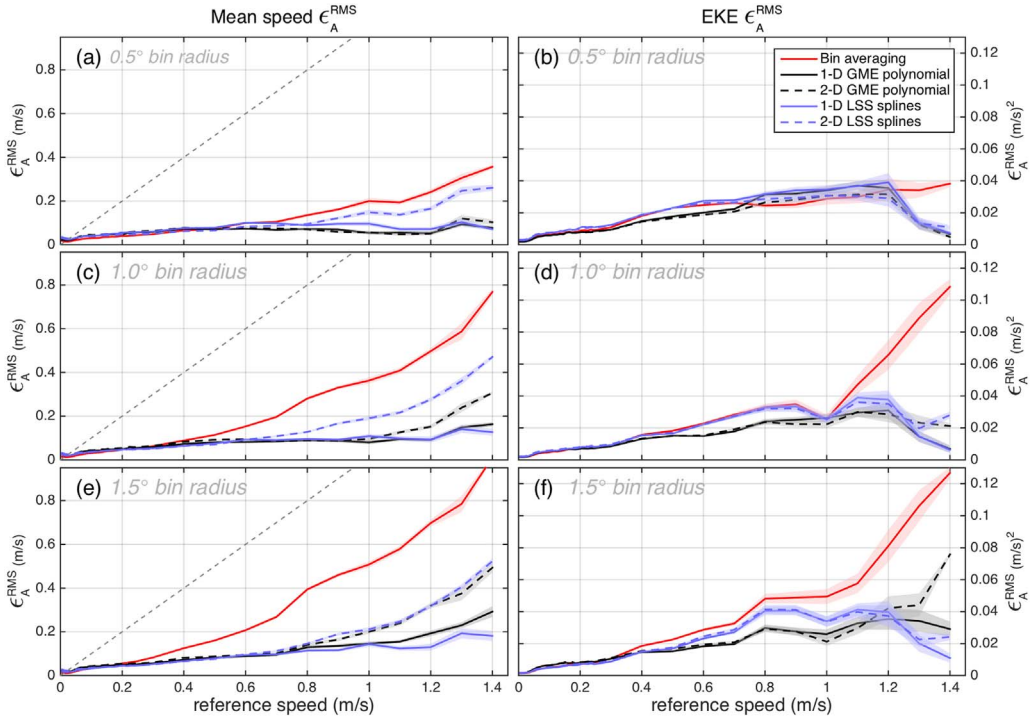

Fig. 8. Same as Fig. 6 for the pseudo-Eulerian mean geostrophic speed (left panels, a, c and e) and the eddy kinetic energy (EKE) (right, b, d and f), considering bin radii equivalent to 0.5° (panels a and b), 1° (c and d) and 1.5° (e and f) degrees longitude. Here, the ϵ_A^{RMS} of both quantities is calculated as a function of the reference Eulerian mean speed. The red, black and blue lines respectively refer to results obtained via bin-averaging (e.g. Fratantoni, 2001), polynomial fitting via Gauss-Markov estimation (GME) (e.g. Lumpkin and Johnson, 2013), and least-squares smoothing splines (LSS) (e.g. Bauer et al., 1998). The solid and dashed lines denote 1-D and 2-D versions of each curve fitting method. (For interpretation of the references to color in this figure legend, the reader is referred to the web version of this article.)

1.3 m/s, the 2-D LSS show larger errors than its 1-D version, reaching maximum values of ~0.03 m^2/s^2 at the 1.4 m/s limit for both 1° and 1.5° radius bins, versus ~0.01 m^2/s^2 for the 1-D LSS.

Comparing 1-D and 2-D GME methods, Fig. 8a shows that, using 0.5° radius bins, the ϵ_A^{RMS} of the mean speed estimates of both versions are similar within 0.02 m/s, with maximum errors of 0.08 and 0.10 m/s, respectively. However, for 1° (1.5°) radius bins (c, e), the errors of the 2-D estimates exceed that of 1-D for reference speeds > 1 (>0.8) m/s, with maximum values of 0.31 (0.49) m/s for 2-D, and of 0.16 (0.29) m/s for 1-D. As for the ϵ_A^{RMS} of EKE estimates (panels b, d and f), the behavior is similar to that described for the LSS, except for the fact that the GME's errors are ~0.01 m^2/s^2 smaller for reference velocities between 0.5 and 1.2 m/s, and that, for 1.5° bin radius, the GME estimates obtained by both 1-D and 2-D GME surpass their LSS correspondents, reaching maximum values of 0.03 and 0.08 m^2/s^2, respectively.

Although the smoothing of mean spatial gradients caused by data binning introduces errors in the residuals, estimates of the seasonal cycle were not impacted by the increasing bin sizes. This is because the functions describing spatial and temporal variations are fitted along different dimensions, implying that errors in retrieving the velocity spatial structure should not significantly affect estimates of the seasonal velocities. However, estimation errors can occur in bins where the sampling is unevenly distributed between the seasons, and/or where seasonal variations have spatial scales smaller than the bin size. Binning also smooths horizontal gradients of the seasonal and eddy variances, albeit less pronounced than for the mean component since both quantities vary over larger scales than the mean velocities. Nevertheless, while this work uses curve fitting methods to model only the spatial structure of the mean, a similar approach could be adopted to describe horizontal gradients of the squared residuals.

In summary, the use of curve fitting methods significantly improves the definition of spatial gradients relative to bin-averaging, where the proposed 1-D approach is less sensitive to smoothing effects than 2-D methods used in previous studies. Regarding differences between 1-D GME and LSS, the LSS fields show smaller errors for larger bin areas. In contrast, the GME fitting reduces biases caused by autocorrelated Lagrangian observations, leading to a better representation of features of the time-mean ocean circulation with speeds of $\mathcal{O}$[0.1 m/s], such as the Loop Current and recirculation cells, while presenting errors similar to LSS for bin radii equal or smaller than 1°. Based on these results and seeking to maximize the number of estimates in sparsely-sampled areas, such as the Southern Ocean and near-equatorial regions, the climatological fields presented here are generated using the 1-D GME method and 1° radius bins.

3.1.4. Error analysis

This Section analyses the spatial distribution of the absolute errors of pseudo-Eulerian estimates (ϵ_A), and investigates whether the standard errors (ϵ_{SE}) calculated via Eq. (7) can be used to estimate ϵ_A.

The left panels of Fig. 9 show global maps of ϵ_A for the pseudo-Eulerian mean (a) and seasonal geostrophic speed (c). Both maps exhibit noisy spatial distributions, suggesting random errors. Conversely, large-scale patterns approximately coincident with the global EKE distribution can be discerned, with larger values marking more energetic regions. Specifically, (a) show errors for the mean speed estimates of 0.02 m/s or smaller for quiescent areas, such as the interior of the subtropical gyres, and of ~0.04–0.09 m/s for energetic regions, as near the equator and in the vicinity of strong current systems, such as western boundary currents and their seaward extensions, the ACC, the Agulhas Retroflection, and the Brazil-Malvinas Confluence. Values above 0.1 m/s are observed in the Indonesian Sea, associated with the low sampling densities in the region, and coinciding with the position of intense time-mean currents. The errors of the seasonal fluctuations in (c) are visibly larger than the errors in the mean, increasing from a base value of ~0.02 m/s at mid oceanic regions to ~0.05–0.14 m/s or larger at energetic regions.

Panels (b) and (d) of Fig. 9 show diagrams of ϵ_A^{RMS} calculated as a function of the square roots of the number of drifter observation days (N) and of the Eulerian EKE, for the mean and seasonal speed estimates, respectively. The diagrams are visually similar, and clearly reveal that the obtained ϵ_A^{RMS} values increase for smaller $N^{1/2}$ and for larger $EKE^{1/2}$, characteristic compatible with theoretical standard errors, which are scaled as function of the ratio $(\sigma^2/N)^{1/2}$.

Fig. 10 compares absolute and standard errors, showing global maps of the ratio ϵ_A/ϵ_{SE} (left panels), and diagrams of the ratio $\epsilon_A^{RMS}/\epsilon_{SE}^{RMS}$ (right), for the pseudo-Eulerian mean (top) and seasonal speed (bottom). Analyzing first the mean speed errors, the ϵ_A/ϵ_{SE} values in panel (a) have mean 1.61 and standard deviation 0.98. Ratios systematically larger than 3 coincide with the position of intense midlatitude currents, such as the Kuroshio and Gulf Stream Currents in the northern hemisphere, and the Agulhas, Brazil and South Indian Ocean Currents in the southern, a possible consequence of the smoothing of horizontal gradients due to data binning. Conversely, values equal or smaller than one are more frequently observed at near-equatorial regions. The $\epsilon_A^{RMS}/\epsilon_{SE}^{RMS}$ values in (b) reveal a more robust relationship between both error metrics, with mean 1.83 and standard deviation 0.48. Near-one ratios are more frequently associated with $N^{1/2}$ between 9.5 and 15 (90-225 drifter days), explaining the prevalence of such values near the equator, a relatively poorly-sampled region (Fig. 1). The discontinuity at $N^{1/2} = 9.5$ is associated with the sampling requirement defined for estimating seasonal fluctuations, whose inclusion in the analysis increases ϵ_{SE}, since more parameters are estimated during the fitting operation.

Considering the errors of the seasonal speed estimates in Fig. 10, the ϵ_A/ϵ_{SE} values in (c) have mean 1.72 and standard deviation 0.49. Coherent spatial features with ratios larger than 2.5 are observed near southeast Asia, along the western coasts of North and South America, the southwestern coast of Africa, and at the center of the North Atlantic subtropical gyre. While the discrepancies near southeast Asia and in the southern hemisphere could hypothetically be attributed to seasonal sampling biases, in the northern hemisphere the observed patterns coincide with some of the most densely sampled regions of the world's oceans. The large ratios in these areas are attributed to the high observational density itself, which acts to reduce the statistical errors due to the increase of the available number of degrees of freedom, combined with the locally low SKE values. The $\epsilon_A^{RMS}/\epsilon_{SE}^{RMS}$ diagram (d) shows suprisingly small variations as a function of $EKE^{1/2}$ and $N^{1/2}$, with mean 1.83 and standard deviation 0.27. The diagram also demonstrates a gradual increase of the ratios as a function of the sampling density for $N^{1/2} > 35$ and $EKE^{1/2} < 0.2$ m/s, reflecting the enhanced ϵ_A/ϵ_{SE} values at the center of the subtropical gyres observed in (c).

If the ϵ_A values in Fig. 9 were purely random and normally-distributed around the reference Eulerian estimates, then about 68.4%, 95.6% and 99.8% of the obtained values would respectively lie within 1, 2 and 3 standard error margins. However, the ratios between ϵ_A and ϵ_{SE} calculated globally (Fig. 10) reveals significantly smaller percentual values (Table 1). Fractions similar to theoretical expectations are only obtained when twice as large standard errors are assumed, in agreement with the mean $\epsilon_A^{RMS}/\epsilon_{SE}^{RMS}$ ratio of 1.83 obtained for both the mean and seasonal speed estimates. This result suggests that the ϵ_{SE} values calculated via Eq. (7) are underestimated by about a factor of 2. This conclusion is valid for the set of optimum parameters used for calculating pseudo-Eulerian quantities in this study, and can vary if different choices are adopted.

For completeness, Fig. 11 shows the global maps of ϵ_A (left panels), and of $EKE^{1/2}$ vs. $N^{1/2}$ diagrams of ϵ_A^{RMS} (right) for pseudo-Eulerian estimates of SKE (top) and EKE (bottom). The spatial distribution of ϵ_A in both maps coincide with the spatial patterns of the corresponding parameters, with errors $< 2.5 \times 10^{-3}$ m^2/s^2 dominating the interior of the basins, increasing to between 1.5 and 4.0×10^{-2} m^2/s^2 in energetic

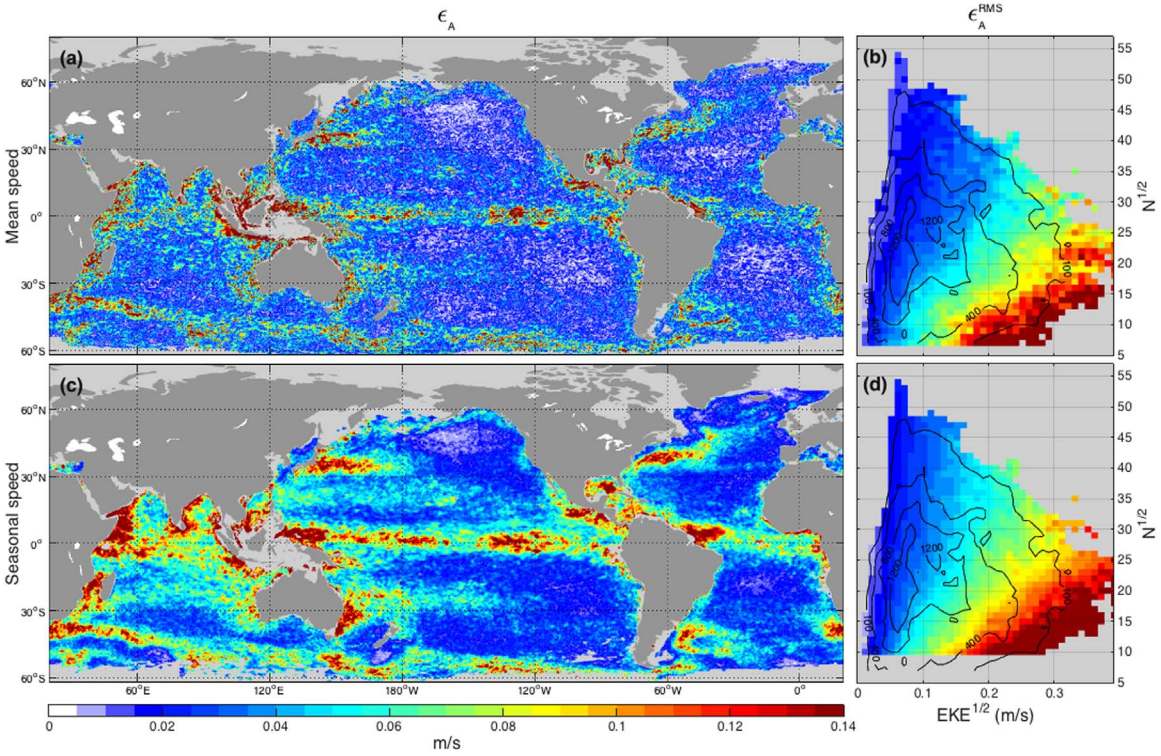

Fig. 9. Panels (a) and (c) respectively show global maps of the absolute errors (ϵ_A) of pseudo-Eulerian mean and seasonal geostrophic speed. The diagrams in (b) and (d) depict the root mean square value of ϵ_A estimates (ϵ_A^{RMS}), subsampled as a function of the square roots of the number of drifter observation days (N) and of the reference Eulerian EKE from the fields in (a) and (c), respectively. The black contours in (b) and (d) delineate the number of ϵ_A values used in the calculation of ϵ_A^{RMS}; gray shading masks regions where the number is smaller than 30.

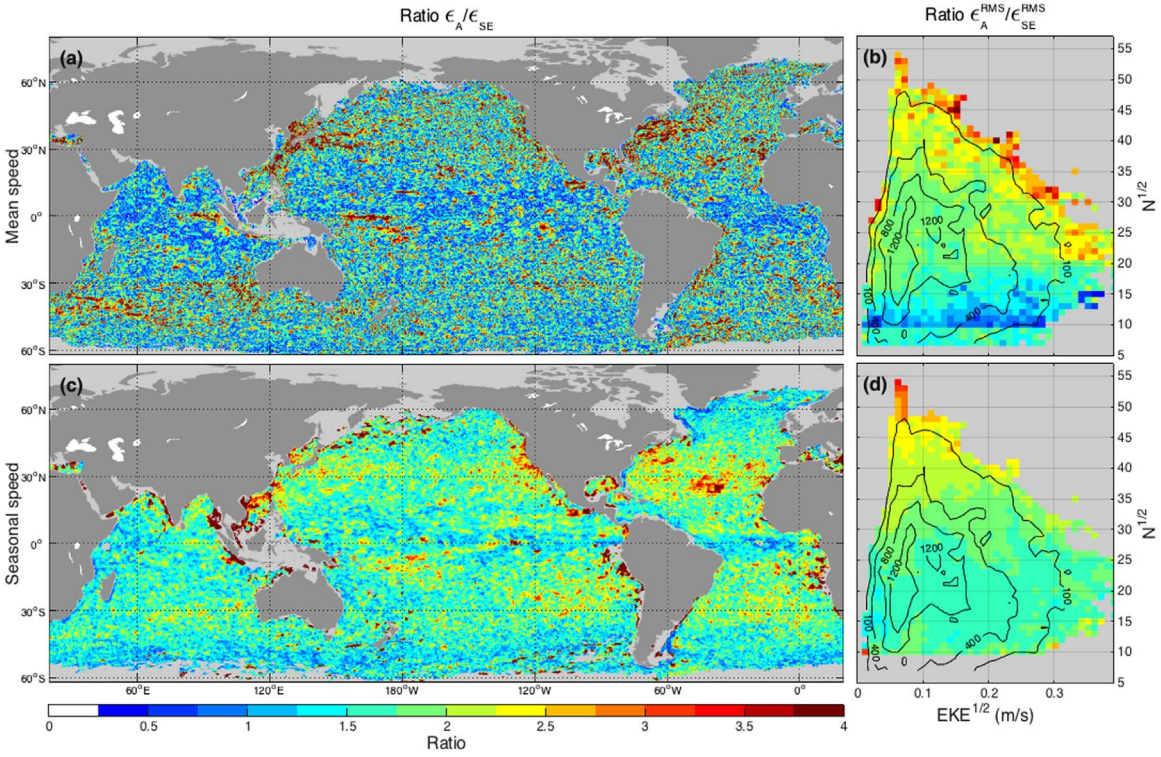

Fig. 10. Similar to Fig. 9, but showing the ratio between absolute (ϵ_A) and standard errors (ϵ_{SE}).

Table 1
Summary of absolute and standard errors (ϵ_A and ϵ_{SE}, respectively) for pseudo-Eulerian mean and seasonal geostrophic velocity estimates, and of the ϵ_A values of the seasonal and eddy variances. Here, $\sqrt{<\epsilon_A^2>}$ and $\sqrt{<\epsilon_P^2>}$ denotes the global root mean square value of each error metric. The percentages are fractions of the global set of ϵ_A values that are smaller than $n_e=1$, 2 and 3 times the corresponding ϵ_{SE} estimates, and twice as large ϵ_{SE} values.

			$\epsilon_A < (n_e \times \epsilon_{SE})$			$\epsilon_A < [n_e \times (2 \times \epsilon_{SE})]$		
	$\sqrt{<\epsilon_A^2>}$	$\sqrt{<\epsilon_{SE}^2>}$	$n_e=1$	$n_e=2$	$n_e=3$	$n_e=1$	$n_e=2$	$n_e=3$
$\bar{u}$	4.11 cm/s	2.95 cm/s	41.3%	70.6%	87.3%	70.6%	95.1%	99.3%
$\bar{v}$	3.64 cm/s	3.13 cm/s	45.6%	76.4%	91.5%	76.4%	97.2%	99.6%
$\sqrt{\bar{u}^2+\bar{v}^2}$	5.49 cm/s	4.30 cm/s	29.3%	71.3%	91.6%	71.3%	97.7%	99.7%
u^s	4.61 cm/s	2.65 cm/s	10.4%	71.5%	94.5%	71.5%	97.4%	98.0%
v^s	4.10 cm/s	2.45 cm/s	13.3%	76.5%	95.6%	76.5%	97.5%	98.0%
$\sqrt{u^{s2}+v^{s2}}$	6.17 cm/s	3.61 cm/s	5.5%	75.3%	96.0%	75.3%	97.6%	98.0%
$<u^{s2}>$	62.32 cm^2/s^2							
$<v^{s2}>$	56.99 cm^2/s^2							
$\frac{1}{2}\times(<u^{s2}>+<v^{s2}>)$	47.52 cm^2/s^2							
$<u^{e2}>$	106.36 cm^2/s^2							
$<v^{e2}>$	110.35 cm^2/s^2							
$\frac{1}{2}\times(<u^{e2}>+<v^{e2}>)$	93.30 cm^2/s^2							

regions. The ϵ_A^{RMS} diagrams reveal that the errors of both SKE and EKE (b and d, respectively) vary as a function of EKE$^{1/2}$ and $N^{1/2}$, although the errors of EKE estimates display a smaller dependency on $N^{1/2}$ for reference EKE$^{1/2}$ values larger than ~0.2 m/s.

3.2. Analysis of the variance bias of undrogued drifter velocity data

As described in Section 2.2, the pseudo-Eulerian variances calculated using slip-corrected velocity data from undrogued drifters surpasses those estimated for drogued instruments by, on average, 36%. This positive bias can stem from factors such as (a) undiagnosed slip, since the simple downwind slip model $\alpha_u \times W$ does not account for wave-induced drifter motion; and (b) the fact that undrogued drifters sample at the surface, implying that their velocity data should include a stronger response to surface-intensified ocean processes, such as Langmuir cells and Ekman currents (Zhurbas et al., 2014). However, maps of the difference between the variances calculated from data of drogued-only and both drogued and undrogued drifters shows spatial patterns and magnitudes similar to the observed in Fig. 11, suggesting that the observed discrepancies may be due to factors unrelated to the water-tracking characteristics of undrogued drifters.

To test this hypothesis, Fig. 12 shows the horizontal and histogram distributions of differences between SKE and EKE estimates calculated using observations from drogued drifters, and using data from both drogued and undrogued drifters. Specifically, panels (a), (b), (e), and (f) are obtained using slip-corrected drifter velocities, while (c), (d), (g) and (h) are from geostrophic velocities interpolated to the drifter locations. Fig. 12 reveals spatial patterns of the SKE and EKE differences

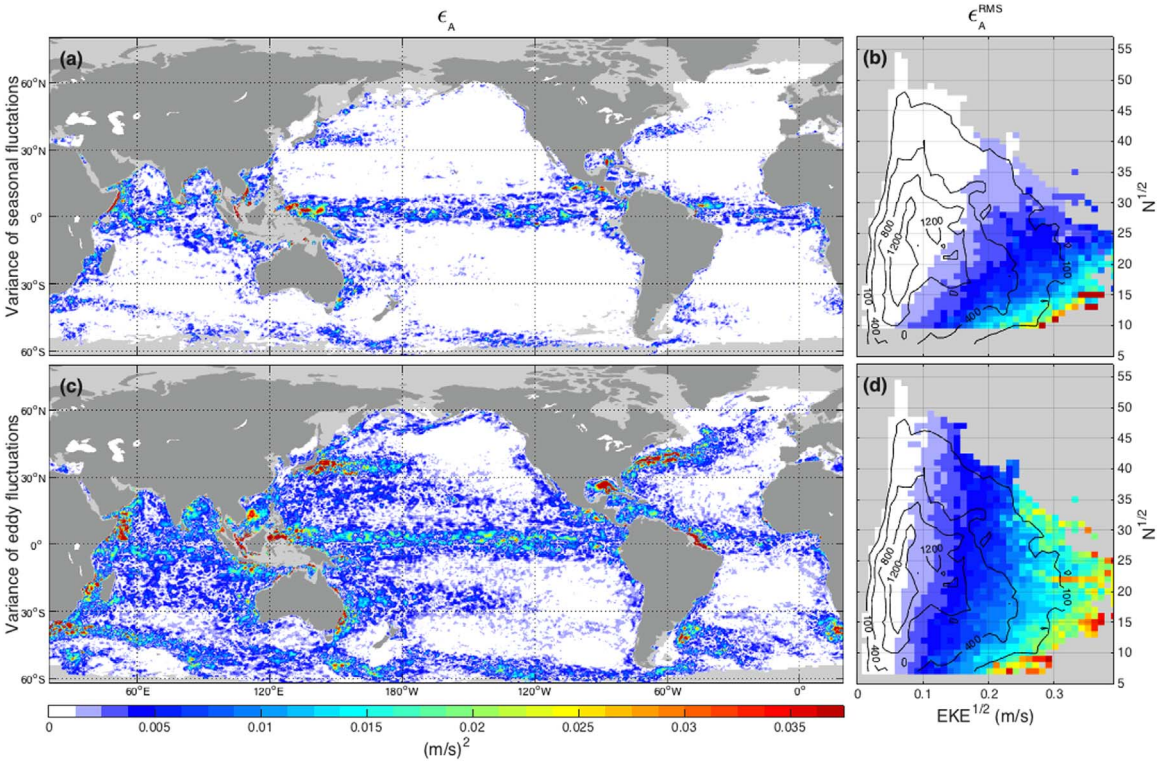

Fig. 11. Similar to Fig. 9, for (a) SKE and (b) EKE.

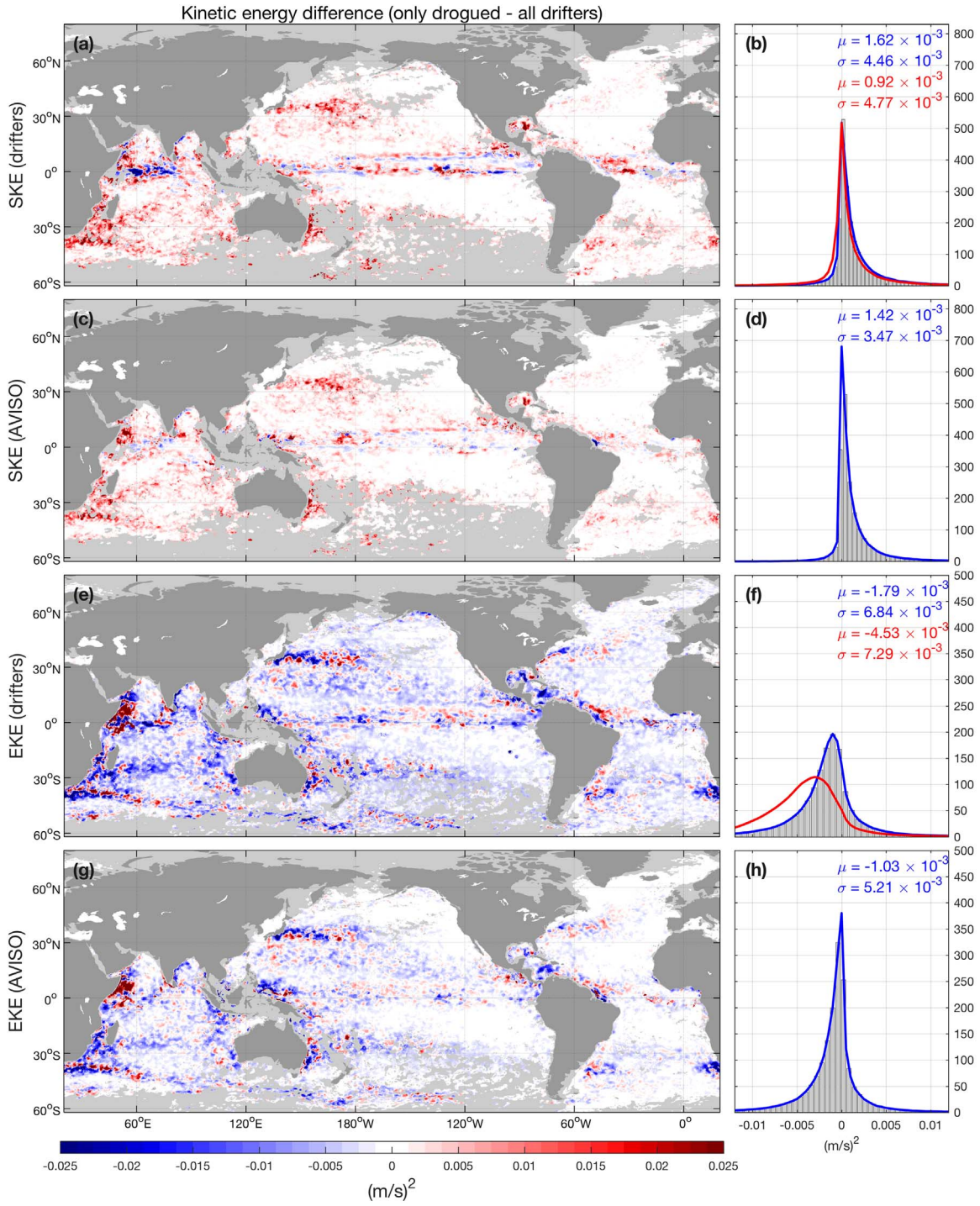

Fig. 12. Difference between the kinetic energy of seasonal fluctuations (SKE) and eddy residuals (EKE) estimated using data from drogued-only and from both drogued and undrogued drifters. The left (right) panels show the spatial (histogram) distribution of the kinetic energy differences, where (a), (b), (e) and (f) are obtained using slip-corrected drifter velocity observations, and (c), (d), (g) and (h) are based on AVISO geostrophic velocities subsampled at the drifter locations. The blue lines overlaid on the histograms are best-fit non-parametric kernel functions, while the red lines correspond to results obtained for drifter velocities not corrected for downwind slip. (For interpretation of the references to color in this figure legend, the reader is referred to the web version of this article.)

visually similar for both Lagrangian datasets. Interestingly, the EKE difference maps (panels e, g) show negative (positive) values at the cyclonic (anticyclonic) regions of the seaward extensions of the Kuroshio, Agulhas and Gulf Stream Currents, which can reflect a preferential sampling of cyclonic (anticyclonic) eddies by drogued (undrogued) drifters (c.f. Lumpkin, 2016). Histogram distributions of the global SKE (EKE) differences are non-Gaussian, being skewed to positive (negative) values and showing long tails. The SKE difference histograms obtained for both Lagrangian datasets are strikingly similar to each other (b, d). Regarding the EKE differences, the histogram for slip-corrected drifter data is flatter and more skewed than that of the AVISO velocities, although it is notably closer to it than the distribution obtained for uncorrected drifter observations (f, h).

The Lagrangian geostrophic velocity dataset is, obviously, not affected by slip biases and by the different sampling depths of drogued and undrogued drifters, meaning that the SKE and EKE differences in panels (c), (d), (g), and (h) of Fig. 12 should reflect effects such as biased sampling, estimation errors conditioned by the smaller sampling

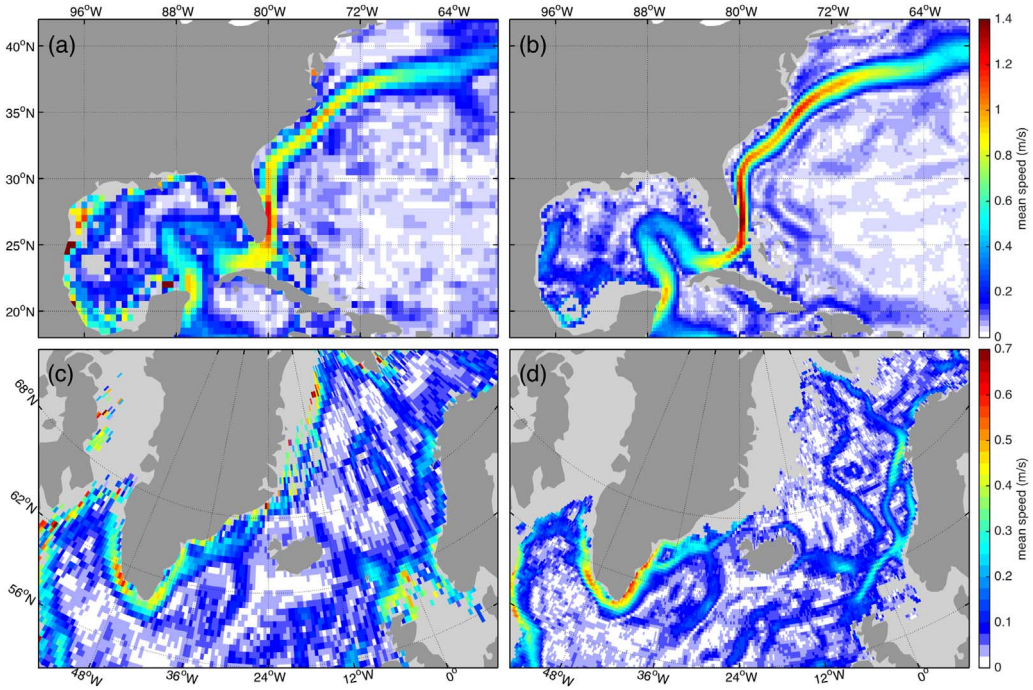

Fig. 13. Pseudo-Eulerian mean speed maps for the Gulf of Mexico and the western North Atlantic (top, panels a and b), and for the Nordic seas (bottom, c and d), calculated from drifter observations. The left panels (a, c) are estimated using the method described in Lumpkin and Johnson (2013), while in the right (b, d) they are obtained via the updated procedure presented in this work.

density of drogued drifters, and errors of the decomposition method. An estimate of the fraction of the variance of the errors in the drifter-based KE estimates, introduced by factors unrelated to the sampling characteristics of undrogued drifters, can be attempted by taking the ratio between the sum of the squares of the SKE (EKE) differences calculated using the Lagrangian geostrophic velocities and the actual drifter measurements, which results in a value of 0.62 (0.57).

3.3. New climatological fields

Fig. 13 shows mean speed maps for the Gulf of Mexico and the western North Atlantic (panels a and b) and for the Nordic Seas (c, d), calculated using drifter observations. Panels (a, c) are the climatology of Lumpkin and Johnson (2013) (version 2.08, generated using GDP drifter observations from February 1979 to March 2016), which fitted 2-D, 2nd degree polynomials via GME to drogued drifter observations selected within elliptical bins, with constant areas of $\pi(2°)^2$, oriented by the declination of the variance ellipse of the eddy fluctuations, and centered at the grid points of a $0.5° \times 0.5°$ global grid. Panels (b, d) are obtained using the method described in Section 2.3.1.

Considering the western North Atlantic and Gulf of Mexico (Fig. 13a, b), the map obtained using the proposed method (b) resolves mean core speeds for the Florida Current and Gulf Stream above 1 m/s between 25 and 37°N, with a maximum speed of 1.57 m/s between the Florida peninsula and the Bahamas, values up to 50% larger than in (a). Furthermore, (b) shows ~0.1 m/s faster Antilles Current and recirculation cells in the eastern flanks of the Antilles and Florida/Gulf Stream Currents, and horizontal scales for all major features closer to those observed in the time-mean Eulerian geostrophic speed map in Fig. 5. The field in (b) also includes coherent circulation patterns not observed in (a), particularly around the Caribbean islands and in the northern flank of the Gulf Stream after the current separates from the coast, north of 36°N.

In the Nordic Seas (Fig. 13c, d), prominent features includes the Norwegian Current, flowing primarily north/northeast along the coast of the Scandinavian peninsula; the clockwise circulation around Greenland, composed of the East and West Greenland Currents; and the southward-flowing Labrador Current, observed at the left edge of the maps. The proposed method (d) produces speeds 0.1–0.2 m/s larger than the climatological field in (c) for all major circulation components, resulting in maximum values of 0.5–0.6 m/s for the East/West Greenland and Labrador Currents, and of 0.35–0.45 m/s for the Norwegian Current. Also, the cross-stream structure of the main features are better defined in (d) and mesoscale details are recovered, such as the currents around Iceland, and an anticyclonic eddy with ~200 km diameter centered at approximately 70°N, 4°W, also resolved in Koszalka et al. (2011) by ensemble-averaging GDP drifter observations grouped within clusters (Koszalka and LaCasce, 2010).

The improvements relative to the results of Lumpkin and Johnson (2013) shown in Fig. 13, are due to (1) the use of smaller bins, which reduces errors for mean velocity estimates caused by the smoothing of the mean horizontal gradients (panel (a) shows horizontal scales and speed magnitudes visually similar to the observed in the pseudo-Eulerian mean geostrophic speed map calculated using the 2-D GME method and 1.5° radii circular bins, presented in Fig. 7); (2) the use of the proposed 1-D curve fitting and of higher-degree polynomials, which reduces the sensitivity of the results to changes in bin size, leading to a better representation of cross-stream velocity gradients; and (3) the inclusion of slip-corrected velocity data from undrogued drifters, which significantly increases the number of observations available for the analysis, particularly in mid-oceanic regions. At basin scales, these factors combined allow resolving mesoscale features of the general circulation. This is illustrated by Fig. 14, which has global pseudo-Eulerian maps obtained from drifter velocity observations and using the proposed decomposition method.

Fig. 14 clearly resolves the major currents composing the gyre and tropical circulation systems. Well-known features, such as the strong equatorial divergence in the Pacific and Atlantic oceans and the convergence in the interior of the subtropical gyres, can be observed in both the meridional velocities (b) and the streamlines (c) (Maximenko et al., 2009, 2012; Lumpkin and Johnson, 2013). Unlike in previous studies, the streamlines are calculated using unsmoothed pseudo-Eulerian mean velocities, indicating the spatial consistency of the results even in regions where the speeds are low (<0.05 m/s).

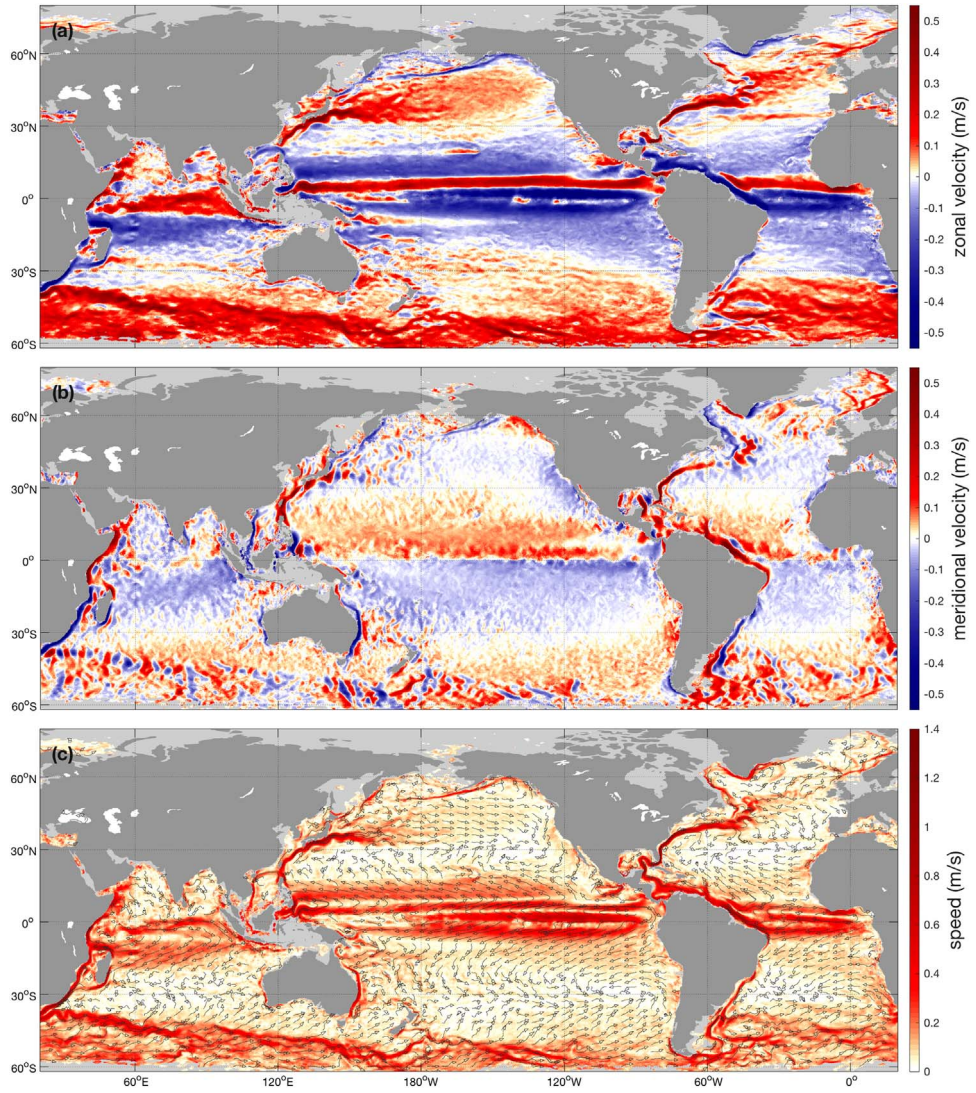

Fig. 14. Global maps of the pseudo-Eulerian mean zonal and meridional velocities (panels a and b, respectively), and of the mean speeds (c), calculated from GDP drifter observations using the decomposition method proposed in this work. The curly vectors in (c) are streamlines calculated using the data depicted in (a) and (b), to indicate the general direction of the large-scale circulation.

Fig. 14 provides a clearer picture of the Antarctic Circumpolar Current (ACC) than in Lumpkin and Johnson (2013), particularly in the Indian and Pacific sectors, due to the inclusion of undrogued drifter data in the analysis (Fig. 1). Prominent features of the ACC absent in the previous climatology includes the southern branch of the ACC in the Indian Ocean between 10 and 80°E, which leads to a narrow "S"-shaped jet crossing the Kerguelen Plateau (55°S, 80°E), downstream of which the ACC merges with the South Indian Ocean Current. In the Pacific sector, two parallel jets are observed between 160 and 120°W, delineating fracture zones of the Antarctic-Pacific ridge. These jets display mean core speeds of up to 0.8 m/s, the largest estimated in the Southern Ocean.

The zonal velocities in Fig. 14a reveal zonally-elongated jet-like features embedded in the large-scale circulation, such as the striation pattern in the South Pacific between 20 and 50°S, which occupies most of the basin's zonal domain. The existence of such features in the ocean was first inferred in the numerical investigation of Treguier et al. (2003). Galperin et al. (2004), based on the results of high-resolution ocean simulations and on similarities of the wavenumber power spectra of oceanic motions to those estimated for the atmospheres of giant planets, argued that banded features should be ubiquitous in the ocean, as a consequence of the tendency of two-dimensional geophysical turbulence to form zonal jets. Observational evidence of their existence in the ocean was first reported by Maximenko et al. (2005) in high-passed altimeter-derived geostrophic velocity fields. Later, Maximenko et al. (2009) used a high-resolution mean dynamic topography model to improve geostrophic velocity estimates from altimeters, obtaining a time-mean map that suggested the existence of quasi-stationary striations in many oceanic regions. Although previous studies also reported the existence of such features in drifter-based mean maps (e.g. Maximenko et al., 2008, 2009), the obtained climatological fields now allow their visualization with a level of detail comparable with that of satellite products.

In the North Atlantic, the eastward flow of the Azores Current can be observed centered at 34°N (Fig. 14a), showing a predominantly zonal flow from approximately 60–6°W. Narrow bands of negative zonal velocities are seen flanking the Azores Current, where the westward flow in its northern flank forms a continuous band of negative velocities with the Gulf Stream's recirculation, seen in the southern limb of the Gulf Stream between 80 and 40°W. West of 50°W, the striation is characterized as elongated bands of alternating positive/negative velocities between 70 and 50°W. This striation connects with the Azores current in the east, and to a narrow band of positive velocities in the northern flank of the Antilles current in the west, forming a continuous pattern of positive zonal velocities from ~76 to 6°W, virtually crossing the North Atlantic basin. Similarly in the North

Pacific, the eastward flow of the Hawaiian Lee Countercurrent (HLCC) is seen centered at ~19°N, extending from 156°W until approximately the dateline (Lumpkin and Flament, 2013). However, another well-resolved band of eastward velocities is observed further west at the same latitude between 130 and 160°E, which can correspond to a westward extension of the HLCC. A narrow band of negative zonal velocities is observed in the northern flank of the HLCC, which is alternated by another band with positive values. Although not well resolved, a visual inspection suggests that the striation pattern continues further north, potentially connecting with the recirculation of the Kuroshio Current's seaward extension. Alternating zonal jets are also prominently observed off the west coast of North America between 22 and 45°N, extending up to 20° longitude towards the basin's interior. These features were described by Centurioni et al. (2008), and are associated with permanent meanders of the California Current. A similar pattern is observed along the west coast of South America from 10 to 35°S. Maximenko et al. (2009) reported striations also off of the west coast of southern Africa, however the low observational density in the region results in a poor definition of the local circulation.

Other notable zonally-elongated features in Fig. 14a, not well resolved in previous drifter-based estimates, includes the eastward velocities off the east coast of South America between 15 and 30°S, extending ~20° longitude seaward within the large-scale, westward flow of the southern branch of the South Equatorial Current (Stramma and Schott, 1999), and possibly associated with recirculation cells of the Brazil Current. Further south, the Zapiola Anticyclone can be observed at 45°S, 42°W (de Miranda et al., 1999; Volkov and Fu, 2008). In the southern Indian Ocean, the eastward flow of the South Indian Ocean Countercurrent (SICC) is seen centered between 24 and 28°S (Siedler et al., 2006; Schott et al., 2009), originating from a recirculation of the Southeast Madagascar Current at ~40°E and observed as a jet until 100°E. The vectors in panel (c) suggests that the SICC merges with the southward flow of the Leeuwin Current (LC) offshore of western Australia at 30°S, 115°E; however the local circulation is not well resolved and the observed branching reflects relatively low observational densities combined with realizations of the eddy field. Finally, Fig. 14 clearly shows the counter-clockwise flow of the LC along the western and southern coasts of Australia (Feng et al., 2009). South of Australia, panel (a) also shows a narrow band of negative zonal velocities in the southern limb of the LC, associated with the Flinders Current (Middleton and Cirano, 2002; Middleton and Bye, 2007).

4. Summary and conclusions

To obtain an improved, global near-surface velocity climatology from GDP drifter observations, this work updates the methods described in Lumpkin and Johnson (2013) by (a) correcting the downwind slip bias of undrogued drifters using a formulation proposed by Pazan and Niiler (2001), an operation that recovers about half of the GDP dataset; and (b) introducing a new method for decomposing drifter data into mean, seasonal and eddy components, designed to minimize the spatial smoothing and smearing effects of other data binning methods. The proposed procedure accounts for spatial variations of the mean within spatial bins by fitting a 1-D, 4th degree polynomial to the binned observations, sorted along a coordinate axis defined at the rotation angle that minimizes the fitting error (Fig. 4).

The correction of the drifter slip bias is done by subtracting a downwind motion from the drifter velocities equal to a fraction α of the ECMWF ERA-Interim 10-m winds. For 15-m drogued drifters, $\alpha_d = 7 \times 10^{-4}$ (Niiler et al., 1995). For undrogued drifters, α_u is calculated via Eq. (1) using data selected within $4° \times 4°$ bins centered at the grid points of a $1° \times 1°$ global grid. Although the obtained α_u values are normally-distributed in probability space, suggesting random fluctuations around the mean, its spatial distribution shows large-scale patterns that are indicative of a geophysical forcing mechanism (Fig. 2). Since (1) does not take into account the fact that undrogued drifters are more sensitive to wave effects, one possibility is that the observed spatial patterns reflect the response of undrogued drifters to a spatially-varying surface gravity wave field.

The correction of the slip motion of undrogued drifters takes into account the spatial variations of α_u by linearly interpolating the obtained values to the drifter locations, producing zonally-averaged, pseudo-Eulerian mean estimates for both drogued and undrogued drifters that are statistically similar across most latitudes (Fig. 3). This also reduces the globally-averaged drogued/undrogued variance ratio from 1.81 to 1.36, where most of the remaining differences can be attributed to factors unrelated to the slip bias of undrogued drifters, such as method errors, the smaller sampling density of drogued drifters, and biased sampling (Fig. 12).

However, it is noted that the linear downwind slip correction for drogued instruments was not validated for wind speeds >10 m/s nor in high wave amplitudes (Niiler et al., 1995), meaning that the slip for both drogued and undrogued drifters can be underestimated in regions with strong winds and/or high wave energy, such as the Southern Ocean. Furthermore, the correction of the slip of undrogued drifters proposed by Eq. (1) operates by removing part of the difference between the along-wind current velocity at 0-m and at 15-m that is correlated with wind speed, which includes not only the wave and wind-induced slip, but also the signature of wind-driven currents such as Ekman flows. Due to the vertical shear of Ekman velocities between the surface and 15-m (c.f. Rio et al., 2014), an undiagnosed cross-wind velocity component associated with the Ekman dynamics can be present in the slip-corrected undrogued drifter velocities, and thus contribute to the differences between the pseudo-Eulerian variances calculated using drogued and undrogued drifter data. Lastly, the α_u estimates have uncertainties of their own, whose origins and magnitude were not accessed, implying that biases due to the use of observations from undrogued drifters can still be significant. Nevertheless, the improvements obtained by the simple correction used in this study are encouraging. If the spatial patterns of α_u truly reflect wave effects, then a more accurate correction can possibly be achieved by first removing the instantaneous Stokes drift from the drifter measurements, estimated from numerical models or satellite/mooring/drifter observations, before calculating the downwind slip coefficient via (1).

The method proposed for the decomposition of Lagrangian data requires definitions for parameters whose adjustment affects the results, including (a) the bin size and mapping resolution; (b) the model used to describe spatial and temporal variations, particularly the polynomial degree n and number of seasonal harmonics m (Eq. (3)); and (c) the decorrelation time scale T_d (Eq. (5)). Those were defined via sensitivity tests using altimeter-derived geostrophic velocity (GV) data from AVISO subsampled at the drifter locations. Specifically, pseudo-Eulerian quantities were calculated from the Lagrangian GV dataset for ranges of the adjustable parameters and compared against the corresponding Eulerian values. This operation resulted in optimum values of $n = 4$, $m = 2$ and $T_d = 6.33$ days, and showed that coherent mesoscale features can be resolved by mapping estimates onto a $0.25° \times 0.25°$ grid.

Regarding bin size, the proposed 1-D approach better resolves the cross-stream velocity structure of narrow currents than other methods, from the $\mathcal{O}$[1 m/s] flow of western boundary currents, to $\mathcal{O}$[0.1 m/s] features such as recirculation cells (Fig. 7), and is less sensitive to variations of this parameter (Fig. 8). The new global climatological fields are generated using 1° radii circular bins, to balance the smoothing effect of binning with the statistical reliability of the estimates in poorly-sampled regions. Fig. 8 shows that this procedure produces mean core speeds for western boundary currents up to 0.2 m/s faster than the decomposition method of Lumpkin and Johnson (2013), 0.4 m/s faster than using 2-D smooth splines (e.g. Bauer et al., 1998; Falco and Zambianchi, 2011), and 0.75 m/s faster than bin-averaging (e.g. Fratantoni, 2001; Jakobsen et al., 2003; Maximenko et al., 2009).

Standard errors, calculated for the modeled velocities via (7), were

compared against the root mean square (RMS) differences between pseudo-Eulerian and Eulerian estimates (absolute errors). Using optimum method parameters, standard errors are found to underestimate absolute errors by about a factor of 2. Differences between both error metrics arise because standard errors do not account for Eulerian binning biases, such as the smoothing of time-mean spatial gradients, and due to possible inadequacies of the model proposed by (3) and (5). The relatively small standard errors can also reflect an underestimation of the decorrelation time scale T_d, which was fixed at all bins assuming a Lagrangian integral time scale of 3 days, when this parameter can actually range from less than one day to $\mathcal{O}$[1 week].

The pseudo-Eulerian mean fields obtained using the presented methods and real drifter observations (Fig. 13) resolves details of the general ocean circulation absent in the climatology described by Lumpkin and Johnson (2013). Core speeds for the Florida/Gulf Stream Currents are up to 50% larger, and recirculation cells and other relatively narrow circulation features are stronger and better-defined. Notably, the global fields also show zonally-elongated striation features in all major oceanic basins (Fig. 14), which previously could only be resolved at such spatial resolution by time-averaging surface velocities inferred from satellite observations (e.g. Maximenko et al., 2009).

These results support the consistency of the obtained mean fields. Since the reliability of the results can be assessed using the standard errors calculated from Eq. (7), this new climatology can be used to validate satellite-derived surface velocity products and the output of realistic numerical simulations. From a methodological standpoint, Peng et al. (2015b) demonstrated that accounting for horizontal velocity gradients improves the convergence of eddy diffusivity estimates, implying that further improvements can possibly be achieved by using the updated decomposition method presented in this study. The better performance of the proposed decomposition method in resolving spatial gradients can also improve estimates of Reynolds stresses, and of the turbulent transport of heat, salt, and tracers across large-scale oceanic fronts. Furthermore, the presented method is general and can be applied to other Lagrangian datasets, such as velocity observations from subsurface floats (e.g. SOFAR and RAFOS), and temperature and salinity data from Argo profilers. Considering that their historical observational density is smaller than that of surface drifters, the better performance of the proposed 1-D approach at larger bin sizes (Fig. 8) can improve the definition of spatial structures for in situ-based climatologies of the subsurface ocean.

Finally, Lumpkin and Johnson (2013) observed that interannual variability correlated with the Southern Oscillation Index (SOI) explained a significant fraction of the near-surface velocity's variance in the tropical Pacific and tropical Indian Oceans. Following that study, the methods described here can be extended to account for forms of interannual variability by including a long-term trend and/or climate indexes as extra functions in the matrix A used in the GME estimation (Eq. (4)). By itself, adding an extra function increases the sampling requirement by one degree of freedom (6 drifter days, assuming a 3-day Lagrangian integral time scale), also increasing the standard errors calculated via Eqs. (6) and (7) due to the larger number of estimated parameters. If the extra function is a climate index such as the SOI, then its successful regression would require the sampling of multiple positive/negative phases of the index, implying that the actual sampling requirements can be significantly larger. For example, Lumpkin and Johnson (2013) estimated the SOI's amplitude in bins with more than 365 drifter days, and other constraints can possibly be further adopted to restrict the estimation to bins where the drifter data is more homogeneously distributed across the years. The expected increase in sampling density promoted by the continued maintenance of the GDP drifter array in the coming years, besides refining the obtained time-mean and seasonal climatological fields, can potentially lead to a better resolution of interannual current variability correlated not only with the SOI, but also with the indexes of other low-frequency climate phenomena, such as the Indian Ocean Dipole and the Atlantic Multi-decadal Oscillation.

Acknowledgements

The authors acknowledge and thank Semyon Grodsky and six anonymous reviewers for their very helpful comments. This work was supported by grants from The Gulf of Mexico Research Initiative, and from the National Science Foundation (OCE Grant 1434198). R. Lumpkin was supported by NOAA's Atlantic Oceanographic and Meteorological Laboratory (AOML) and the Climate Program Office. The global near-surface current climatology described here is publicly available through the Gulf of Mexico Research Initiative Information & Data Cooperative (GRIIDC) at https://data.gulfresearchinitiative.org (doi: http://dx.doi.org/10.7266/N7SJ1HN5), and through NOAA/AOML at http://www.aoml.noaa.gov/phod/dac/dac_meanvel.php.

References

Bauer, S., Svenson, M.S., Griffa, A., Mariano, A.J., Owens, K., 1998. Eddy-mean flow decomposition and eddy-diffusivity estimates in the tropical Pacific Ocean: 1. Methodology. J. Geophys. Res., 103, 30,855–30,871. http://dx.doi.org/10.1029/1998JC900009.

Beron-Vera, F.J., Olascoaga, M.J., Lumpkin, R., 2016. Inertia-induced accumulation of flotsam in the subtropical gyres. Geophys. Res. Lett. 43. http://dx.doi.org/10.1002/2016GL071443.

Castelão, G.P., Johns, W.E., 2011. Sea surface structure of North Brazil Current rings derived from shipboard and moored acoustic Doppler current profiler observations. J. Geophys. Res. 116. http://dx.doi.org/10.1029/2010JC006575.

Centurioni, L.R., Ohlmann, J.C., Niiler, P.P., 2008. Permanent meanders in the California Current System. J. Phys. Oceanogr., 38, 1690–1710. http://dx.doi.org/10.1175/2008JPO3746.1.

Chelton, D.B., Schlax, M.G., Samelson, R.M., de Szoeke, R.A., 2007. Global observations of large oceanic eddies. Geophys. Res. Lett. 34. http://dx.doi.org/10.1029/2007GL030812.

de Miranda, A.P., Barnier, B., Dewar, W.K., 1999. On the dynamics of the Zapiola Anticyclone. J. Geophys. Res., 104, 21,137–21,149. http://dx.doi.org/10.1029/1999JC900042.

Dee, D.P., Uppala, S.M., Simmons, A.J., Berrisford, P., Poli, P., Kobayashi, S., Andrae, U., Balmaseda, M.A., Balsamo, G., Bauer, P., Bechtold, P., Beljaars, A.C.M., van de Berg, L., Bidlot, J., Bormann, N., Delsol, C., Dragani, R., Fuentes, M., Geer, A.J., Haimberger, L., Healy, S.B., Hersbach, H., Hólm, E.V., Isaksen, L., Kållberg, P., Köhler, M., Matricardi, M., McNally, A.P., Monge-Sanz, B.M., Morcrette, J.J., Park, B.K., Peubey, C., de Rosnay, P., Tavolato, C., Thépaut, J.N., Vitart, F., 2011. The ERA-Interim reanalysis: configuration and performance of the data assimilation system. Q. J. R. Meteorol. Soc. 137, 553–597. http://dx.doi.org/10.1002/qj.828.

Ducet, N., Le Traon, P.Y., 2001. A comparison of surface eddy kinetic energy and Reynolds stresses in the Gulf Stream and the Kuroshio Current systems from merged TOPEX/Poseidon and ERS-1/2 altimetric data. J. Geophys. Res., 106, 16,603–16,622. http://dx.doi.org/10.1029/2000JC000205.

Ducet, N., Le Traon, P.Y., Reverdin, G., 2000. Global high-resolution mapping of ocean circulation from TOPEX/Poseidon and ERS-1 and -2. J. Geophys. Res., 105, 19, 477–19,498. http://dx.doi.org/10.1029/2000JC900063.

Falco, P., Zambianchi, E., 2011. Near-surface structure of the Antarctic Circumpolar Current derived from World Ocean Circulation Experiment drifter data. J. Geophys. Res. 116. http://dx.doi.org/10.1029/2010JC006349.

Feng, M., Weller, E., Hill, K., 2009. The Leeuwin Current, in: Poloczanska, E., Hobday, A., Richardson, A. (Eds.), A Marine Climate Change Impacts and Adaptation Report Card for Australia 2009. NCCARF Publication 05/09. ISBN 978-1-921609-03-9.

Fratantoni, D., 2001. North Atlantic surface circulation during the 1990's observed with satellite-tracked drifters. J. Geophys. Res., 106, 2,2067–2,2093. http://dx.doi.org/10.1029/2000JC000730.

Galperin, B., Nakano, H., Huang, H.P., Sukoriansky, S., 2004. The ubiquitous zonal jets in the atmospheres of giant planets and Earth's oceans. Geophys. Res. Lett. 31, L13303. http://dx.doi.org/10.1029/2004GL019691.

Grodsky, S.A., Lumpkin, R., Carton, J.A., 2011. Spurious trends in global surface drifter currents. Geophys. Res. Lett. 38, L10606. http://dx.doi.org/10.1029/2011GL047393.

Hansen, D., Poulain, P.M., 1996. Quality controland interpolations of WOCE-TOGA drifter data. J. Atmos. Ocean. Technol., 900–909. (doi: http://dx.doi.org/10.1175/1520-0426(1996)013 < 0900:QCAIOW > 2.0.CO;2).

Huang, H.P., Kaplan, A., Curchitser, E.N., Maximenko, N.A., 2007. The degree of anisotropy for mid-ocean currents from satellite observations and an eddy-permitting model simulation. J. Geophys. Res. 112. http://dx.doi.org/10.1029/2007JC004105.

Inoue, H., 1986. A least-squares smooth fitting for irregularly spaced data: Finite-element approach using the cubic B-spline basis. Geophysics, 51, 2,051–2,066. http://dx.doi.org/10.1190/1.1442060.

Jakobsen, P.K., Ribergaard, M.H., Quadfasel, D., Schmith, T., Hughes, C.W., 2003. Near-surface circulation in the northern North Atlantic as inferred from Lagrangian

drifters. J. Geophys. Res. 108. http://dx.doi.org/10.1029/2002JC001554.
Johnson, G.C., 2001. The Pacific ocean subtropical cell surface limb. Geophys. Res. Lett., 28, 1771–1774. http://dx.doi.org/10.1029/2000GL012723.
Koszalka, I., LaCasce, J.H., 2010. Lagrangian analysis by clustering. Ocean Dyn. 60, 957–972. http://dx.doi.org/10.1007/s10236-010-0306-2.
Koszalka, I., LaCasce, J.H., Andersson, M., Orvik, K.A., Mauritzen, C., 2011. Surface circulation in the Nordic Seas from clustered drifters. Deep-Sea Res. I 58, 468–485. http://dx.doi.org/10.1016/j.dsr.2011.01.007.
LaCasce, J.H., 2008. Statistics from Lagrangian observations. Progress. Oceanogr. 77, 1–29. http://dx.doi.org/10.1016/j.pocean.2008.02.002.
Lagerloef, G.S.E., Mitchum, G.T., Lukas, R.B., Niiler, P.P., 1999. Tropical Pacific near-surface currents estimated from altimeter, wind and drifter data. J. Geophys. Res., 104, 23,313–23,326. http://dx.doi.org/10.1029/1999JC900197.
Lumpkin, R., 2003. Decomposition of surface drifter observations in the tropical Atlantic Ocean. Geophys. Res. Lett. 14, 1,753. http://dx.doi.org/10.1029/2003GL017519.
Lumpkin, R., Flament, P.J., 2013. Extent and energetics of the Hawaiian Lee Countercurrent. Oceanography 26, 58–65. http://dx.doi.org/10.5670/oceanog.2013.05.
Lumpkin, R., Grodsky, S.A., Centurioni, L., Rio, M.H., Carton, J.A., Lee, D., 2013. Removing spurious low-frequency variability in drifter velocities. J. Atmos. Ocean. Technol. 30, 353–360. http://dx.doi.org/10.1175/JTECH-D-12-00139.1.
Lumpkin, R., 2016. Global trajectories of coherent vortices from surface drifter trajectories. J. Geophys. Res.: Oceans, 121, 1,306–1,321. http://dx.doi.org/10.1002/2015JC011435.
Lumpkin, R., Johnson, G., 2013. Global ocean surface velocities from drifters: mean, variance, ENSO response, and seasonal cycle. J. Geophys. Res., 118, 2,992–3,006. http://dx.doi.org/10.1002/jgrc.20210.
Lumpkin, R., Pazos, M., 2007. Measuring surface currents with Surface Velocity Program drifters: the instrument, its data and some recent results. In: Griffa, A., Kirwan, A., Mariano, A., Özgökmen, T., Rossby, T. (Eds.), Lagrangian Analysis and Prediction of Coastal and Ocean Dynamics, Cambridge University Press. Chapter 2, pp. 39–67.
Mariano, A.J., Ryan, E.H., 2007. Lagrangian analysis and prediction of coastal and ocean dynamics (LAPCOD review). In: Griffa, A., Kirwan, A.D., Mariano, A.J., Özgökmen, T., Rossby, T. (Eds.), Lagrangian Analysis and Prediction of Coastal and Ocean Dynamics, Cambridge University Press. Chapter 13, pp. 423–479.
Maximenko, N.A., Bang, B., Sasaki, H., 2005. Observational evidence of alternating jets in the world ocean. Geophys. Res. Lett. 32. http://dx.doi.org/10.1029/2005GL022728.
Maximenko, N.A., Hafner, J., Niiler, P.P., 2012. Pathways of marine debris derived from trajectories of Lagrangian drifters. Mar. Pollut. Bull. 65, 51–62. http://dx.doi.org/10.1016/j.marpolbul.2011.04.016.
Maximenko, N.A., Melnichenko, O.V., Niiler, P.P., Sasaki, H., 2008. Stationary mesoscale jet-like features in the ocean. Geophys. Res. Lett. 35. http://dx.doi.org/10.1029/2008GL033267.
Maximenko, N.A., Centurioni, L.R., Lumpkin, R., 2013. Ocean surface circulation. In: Ocean Circulation and Climate: A 21st Century Perspective, volume 103. Chapter 12, pp. 283–304.
Maximenko, N.A., Niiler, P.P., Rio, M., Melnichenko, O., Centurioni, L., Chambers, D., Zlotnicki, V., Galperin, B., 2009. Mean dynamic topography of the ocean derived from satellite and drifting buoy data using three different techniques. J. Atmos. Ocean. Technol., 26, 1,910–1,918. http://dx.doi.org/10.1175/2009JTECHO672.1.
Middleton, J.F., Cirano, M., 2002. A northern boundary current along Australia's southern shelves: the Flinders Current. J. Geophys. Res. 107, 3129. http://dx.doi.org/10.1029/2000JC000701.
Middleton, J.F., Bye, J.A.T., 2007. A review of the shelf-slope circulation along Australia's southern shelves: Cape Leeuwin to Portland. Progress. Oceanogr. 75, 1–41. http://dx.doi.org/10.1016/j.pocean.2007.07.001.
Niiler, P.P., 2001. The world ocean surface circulation. In: Siedler, G., Church, J., Gould, J. (Eds.), Ocean Circulation and Climate, Academic Press, San Diego, California. volume 77 of International Geophysical Series, pp. 193–204.
Niiler, P.P., Sybrandy, A.S., Kenong, B., Poulain, P.M., Bitterman, D., 1995. Measurements of the water-following capability of holey-sock and tristar drifters. Deep-Sea Res. I, 42, 1,961-1,964. http://dx.doi.org/10.1016/0967-0637(95)00076-3.
Pazan, S.E., Niiler, P.P., 2001. Recovery of near-surface velocity from undrogued drifters. J. Atmos. Ocean. Technol., 18, 476–489. (http://dx.doi.org/10.1175/1520-0426(2001)018 < 0476:RONSVF > 2.0.CO;2).
Peng, S., Qian, Y.K., Lumpkin, R., Du, Y., Wang, D., Li, P., 2015a. Characteristics of the near-surface currents in the Indian Ocean as deduced from satellite-tracked surface drifters. Part I: pseudo-Eulerian statistics. J. Phys. Oceanogr. 45, 441–458. http://dx.doi.org/10.1175/JPO-D-14-0050.1.
Peng, S., Qian, Y.K., Lumpkin, R., Li, P., Wang, D., Du, Y., 2015b. Characteristics of the near-surface currents in the Indian Ocean as deduced from satellite-tracked surface drifters. Part II: Lagrangian statistics. J. Phys. Oceanogr. 45, 459–477. http://dx.doi.org/10.1175/JPO-D-14-0049.1.
Perez, R.C., Hormann, V., Lumpkin, R., Brandt, P., Johns, W.E., Hernandez, F., Schmid, C., Bourlès, B., 2014. Mean meridional currents in the central and eastern equatorial Atlantic. Ocean Dyn., 43, 2,943–2,962. http://dx.doi.org/10.1007/s00382-013-1968-5.
Poje, A.C., Özgökmen, T.M., Lipphard, B.L., Haus, B.K., Ryan, E.H., Haza, A.C., Jacobs, G.A., Reniers, A.J.H.M., Olascoaga, M.J., Novelli, G., Griffa, A., Beron-Vera, F.J., Chen, S.S., Coelho, E., Hogan, P.J., Kirwan, A.D., Huntley, H.S., Mariano, A.J., 2014. Submesoscale dispersion in the vicinity of the Deepwater Horizon spill. Proc. Natl. Acad. Sci. USA, 111, 12,693–12,698. http://dx.doi.org/10.1073/pnas.1402452111.
Polito, P.S., Sato, O.T., 2015. Do eddies ride on Rossby waves? J. Geophys. Res. Oceans, 120, 5,417–5,435. http://dx.doi.org/10.1002/2015JC010737.
Poulain, P.M., Gerin, R., Maurin, E., Pennel, R., 2009. Wind effects on drogued and undrogued drifters in the eastern Mediterranean. J. Atmos. Ocean. Technol., 26, 1, 144–1,156. http://dx.doi.org/10.1175/2008JTECHO618.1.
Reverdin, G., Niiler, P.P., Valdimarsson, H., 2003. North Atlantic Ocean surface currents. J. Geophys. Res. 108. http://dx.doi.org/10.1029/2001JC001020.
Richardson, P.L., Walsh, D., 1986. Mapping climatological seasonal variations of surface currents in the tropical Atlantic using ship drifts. J. Geophys. Res., 91, 10,537–10,550. http://dx.doi.org/10.1029/JC091iC09p10537.
Rio, M.H., Mulet, S., Picot, N., 2014. Beyond GOCE for the ocean circulation estimate: synergetic use of altimetry, gravimetry, and in situ data provides new insight into geostrophic and Ekman currents. Geophys. Res. Lett. 41, 8,918–8,925. http://dx.doi.org/10.1002/2014GL061773.
Schott, F.A., Xie, S., McCreary Jr., J.P., 2009. Indian Ocean circulation and climate variability. Rev. Geophys. 47. http://dx.doi.org/10.1029/2007RG000245.
Siedler, G., Rouault, M., Lutjeharms, J.R.E., 2006. Structure and origin of the subtropical South Indian Ocean Countercurrent. Geophys. Res. Lett. 33. http://dx.doi.org/10.1029/2006GL027399.
Stramma, L., Schott, F., 1999. The mean flow field of the tropical Atlantic. Deep-Sea Res. II 46, 279–303. http://dx.doi.org/10.1016/S0967-0645(98)00109-X.
Treguier, A.M., Hogg, N.G., Maltrud, M., Speer, K., Thierry, V., 2003. The origin of deep zonal flows in the Brazil Basin. J. Phys. Oceanogr., 33, 580–599. (http://dx.doi.org/10.1175/1520-0485(2003)033 < 0580:TOODZF > 2.0.CO;2).
Volkov, D.L., Fu, L.L., 2008. The role of vorticity fluxes in the dynamics of the Zapiola Anticyclone. J. Geophys. Res. 113. http://dx.doi.org/10.1029/2008JC004841.
Wunsch, C., 1996. The Ocean Circulation Inverse Problem. Cambridge Univ. Press, New York, pp. 442.
Zhurbas, V., Lyzhkov, D., Kuzmina, N., 2014. Drifter-derived estimates of lateral eddy diffusivity in the World Ocean with emphasis on the Indian Ocean and problems of parameterisation. Deep-Sea Res. I 83, 1–11. http://dx.doi.org/10.1016/j.dsr.2013.09.001.